Title

Turbulent convection in rapidly rotating spherical shells: A model for equatorial and high latitude jets on Jupiter and Saturn

Journal

Icarus, 187(2)

ISSN

0019-1035

Authors

Heimpel, Moritz
Aurnou, Jonathan

Publication Date

2007-04-01

DOI

10.1016/j.icarus.2006.10.023

Peer reviewed

Available online at www.sciencedirect.com
ScienceDirect
Icarus 187 (2007) 540–557
ICARUS
www.elsevier.com/locate/icarus

Turbulent convection in rapidly rotating spherical shells: A model for equatorial and high latitude jets on Jupiter and Saturn

Moritz Heimpel [a,*], Jonathan Aurnou [b]

[a] *Department of Physics, University of Alberta, Edmonton, Alberta, Canada T6G 2J1*
[b] *Department of Earth and Space Sciences, University of California, Los Angeles, CA 90095-1567, USA*

Received 1 October 2005; revised 13 October 2006

Available online 15 December 2006

Abstract

The origin of zonal jets on the jovian planets has long been a topic of scientific debate. In this paper we show that deep convection in a spherical shell can generate zonal flow comparable to that observed on Jupiter and Saturn, including a broad prograde equatorial jet and multiple alternating jets at higher latitudes. We present fully turbulent, 3D spherical numerical simulations of rapidly rotating convection with different spherical shell geometries. The resulting global flow fields tend to be segregated into three regions (north, equatorial, and south), bounded by the tangent cylinder that circumscribes the inner boundary equator. In all of our simulations a strong prograde equatorial jet forms outside the tangent cylinder, whereas multiple jets form in the northern and southern hemispheres, inside the tangent cylinder. The jet scaling of our numerical models and of Jupiter and Saturn is consistent with the theory of geostrophic turbulence, which we extend to include the effect of spherical shell geometry. Zonal flow in a spherical shell is distinguished from that in a full sphere or a shallow layer by the effect of the tangent cylinder, which marks a reversal in the sign of the planetary β-parameter and a jump in the Rhines length. This jump is manifest in the numerical simulations as a sharp equatorward increase in jet widths—a transition that is also observed on Jupiter and Saturn. The location of this transition gives an estimate of the depth of zonal flow, which seems to be consistent with current models of the jovian and saturnian interiors.

Keywords: Jupiter; Saturn; Atmospheres, dynamics; Interiors

1. Introduction

From spacecraft and ground-based observations of cloud motions in the upper atmospheres of the jovian planets (Jupiter, Saturn, Uranus and Neptune), it is known that their surface winds are dominated by zonal (i.e., longitudinally directed) motions. Detailed information on the wind patterns of Jupiter and Saturn, including time variability, has been provided by the Voyager missions, the Cassini spacecraft (which is currently in orbit about Saturn), and the Hubble space telescope (Porco et al., 2003, 2005; Sanchez-Lavega et al., 2004; Vasavada and Showman, 2005). Each of the four jovian planets exhibits a system of jets with latitudinally varying winds that alternate between prograde and retrograde flow with respect to the apparent mean planetary rotation (e.g., Giampieri and Dougherty, 2004; Russell et al., 2001). Jupiter and Saturn both feature strong prograde (eastward) equatorial jets and a system of smaller-scale, higher latitude jets that flow in alternating relative directions (Fig. 1). In Jupiter's equatorial region, which includes latitudes within roughly $\pm 25°$, a strong prograde equatorial jet is flanked by a similarly powerful prograde jet to the north and a strong asymmetrically retrograde jet to the south. The undulating zonal flow that defines the higher latitude jets has lower amplitude and shorter wavelength than the equatorial flow. Saturn's zonal latitudinal flow profile features a single equatorial jet extending to roughly $\pm 35°$ in latitude, with three higher-latitude prograde jets in each hemisphere.

Equatorial wind speeds on Jupiter exceed 100 m/s, and Saturn's equatorial jet reaches speeds of over 400 m/s. These represent some of the highest sustained wind speeds in the Solar System. However, the large size and rapid rotation of Jupiter and Saturn means that these flow speeds are small relative to the surface velocity of planetary rotation. The Rossby number,

* Corresponding author. Fax: +1 780 492 0714.
E-mail address: mheimpel@phys.ualberta.ca (M. Heimpel).

0019-1035/$ – see front matter
doi:10.1016/j.icarus.2006.10.023

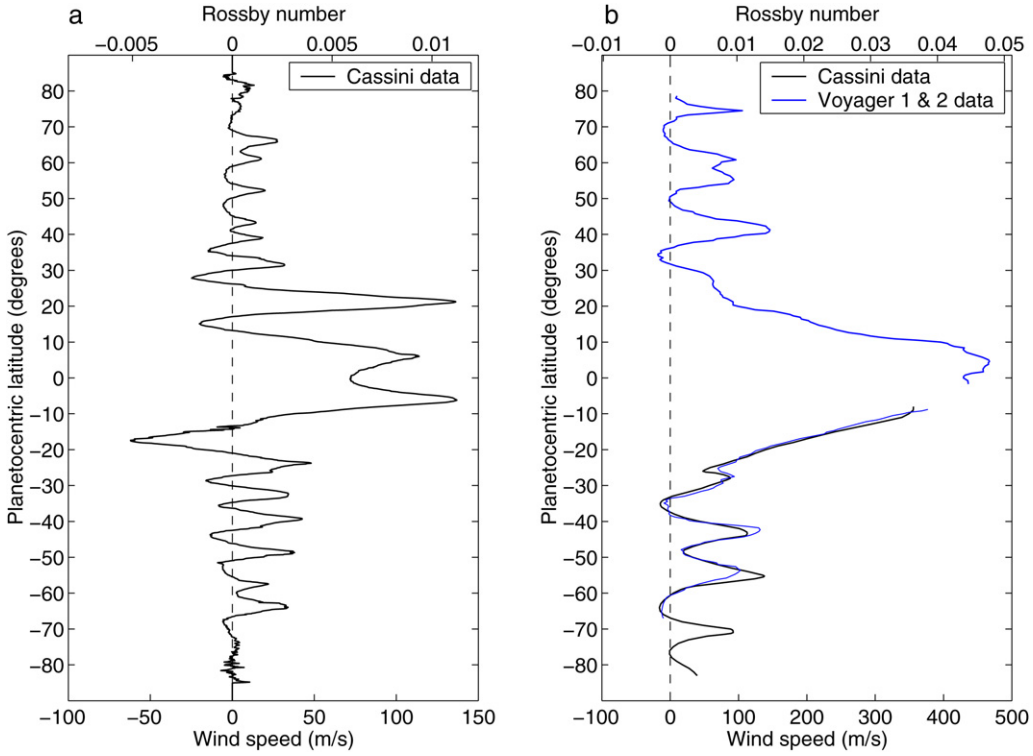

Fig. 1. Surface wind profiles from observations of (a) Jupiter and (b) Saturn. Conversion between wind velocities u (in m/s) and the non-dimensional Rossby number is given by $Ro = u/(\Omega r_o)$, where Ω is the planetary rotation rate and r_o is the planetary radius to the upper cloud deck. Cassini Jupiter data [black curve, panel (a)] and Saturn data [black curve, panel (b)] kindly provided by Ashwin Vasavada. Voyager 1 & 2 Saturn data [blue curve in (b)] from Sanchez-Lavega et al. (2000). (For interpretation of the references to color in this figure ledend, the reader is referred to the web version of this article.)

which gives a non-dimensional measure of the relative importance of flow inertia to planetary rotation, is defined by $Ro = U/(\Omega r_o)$, where U scales the flow speed, Ω and r_o are the planetary angular velocity and radius, respectively. The peak observable Rossby numbers for Jupiter ($Ro \simeq 0.012$) and Saturn ($Ro \simeq 0.045$) imply that the flow dynamics on both planets are strongly dominated by the effects of planetary rotation. The surface winds on Saturn seem to be shifted strongly toward the prograde direction. However, we note that an apparent change in the period of Saturn's kilometric radio (SKR) emissions (which are used to estimate planetary rotation rate), suggests that the planetary rotation rate is uncertain. An increase of roughly 1% in the period of SKR emissions is observed between the Voyager and Cassini space missions (Sanchez-Lavega, 2005; Porco et al., 2005). Since surface velocity measurements are taken with respect to the estimated rotation rate, and considering that surface flow velocities are low compared to the rotational velocity, a 1% uncertainty in rotation rate leads to a very substantial (roughly 20%) uncertainty in the surface zonal wind speed.

In contrast to the prograde equatorial winds of Jupiter and Saturn, Uranus and Neptune each have a strong retrograde equatorial jet, with a single high-latitude prograde jet in each hemisphere (Hammel et al., 2005; Sanchez-Lavega et al., 2004). The magnitude of the equatorial wind speed of Neptune is comparable to that of Saturn. However, because the "Ice Giants" are smaller and have a slower rotation rate, their Rossby numbers, though still low compared to unity, are significantly higher than for Jupiter and Saturn, with Neptune's equatorial jet exceeding $Ro \simeq 0.1$. In this paper we will focus mainly on the dynamics of Jupiter and Saturn.

Measurements of Jupiter's atmosphere from the Galileo probe in 1995 represent the only direct observations of atmospheric wind speed below the upper cloud deck. Those Doppler velocity measurements determined an increase in the wind speed from 80 to 160 m/s with depth in the interval 1–4 bar. The wind speed then remained constant with depth to a pressure of 22 bar (Atkinson et al., 1998), which corresponds to several atmospheric scale heights and roughly 150 km beneath the cloud deck. This implies that the winds of Jupiter extend well below the tropospheric weather layer, which is based at 5–10 bars. However, because the probe entered an equatorial "hot spot," which may represent anomalous atmospheric flow, it is questionable whether these measurements are representative of the global wind profile (Ingersoll et al., 2004).

Additional evidence relating to the origin of atmospheric flow on the jovian planets comes from thermal emission data and models for the deep planetary interiors. The emitted heat flux of Jupiter and Saturn is relatively constant with latitude. The outward heat from each planet accounts for roughly 1.7 times the absorbed solar heat (Ingersoll, 1976; Pirraglia, 1984). This suggests that the zonal winds may be driven by deep convection, since there are comparable amounts of solar and internal energy available to drive large-scale flow (Ingersoll and Pollard, 1982).

The outer fluid layers of Jupiter and Saturn undergo a phase transition with depth from molecular to metallic hydrogen. The sharpness of this transition is highly uncertain. Jupiter may still be undergoing active differentiation so that the transition is gradual, whereas Saturn, which is colder and further along in its differentiation history, may have a sharp phase boundary at greater depth (Guillot et al., 2004). Although the details of the phase relations in the molecular H_2–He envelope may have a rich and complicated structure we will refer to this layer simply as the "deep atmosphere." The liquid metal interior is thought to be the generating region of the strong magnetic fields of Jupiter and Saturn. The metalization transition has been estimated to occur at 0.80 to 0.85 of Jupiter's radius. These bounding estimates represent the maximum depth of the fast zonal flow layer because zonal motions are thought to be relatively slow within the metallic core.

It is likely that fast zonal flow would be attenuated by electromagnetic torque resulting from a strong electrical conductivity gradient at depths shallower than the metalization transition (Kirk and Stevenson, 1987; Guillot et al., 2004). The strong magnetic fields of Jupiter and Saturn affect the weakly conducting lower regions of the deep atmosphere. Zonal flows in this region would tend to shear out the magnetic field. This shearing will be resisted by Lorentz forces. Such a magnetic braking effect has been documented in a number of geodynamo simulations (Christensen et al., 1999; Busse, 2002; Wicht, 2002). Non-magnetic numerical simulations (such as those presented here) feature relatively large percentages of zonal kinetic energy (Aurnou and Olson, 2001; Christensen, 2001, 2002). In magnetoconvection and dynamo cases, however, the zonal energy is vastly reduced even when the poloidal convective motions are facilitated by the presence of the magnetic field (Christensen et al., 1999). The depth at which magnetic braking would be significant is unknown, but has been estimated at 0.85–0.95 of Jupiter's radius (Guillot et al., 2004). Thus we assume a reasonable range of depth estimates of fast zonal flow to be 0.85–0.95 of Jupiter's radius. For Saturn, lesser gravity means that the deep atmospheric layer depth is greater. It follows that corresponding estimates for the level to which fast zonal flow extends in Saturn are 0.6–0.85 of its radius.

Another possible mechanism for decreasing the zonal flow with depth is the strongly increasing density due to compression and phase changes at depth. It has been suggested that, taking into account fluid compression, the mass flux ρu would be a conserved quantity on axial cylinders (Christensen, 2002). This is in contrast to the Boussinesq case, where the Taylor–Proudman theorem ensures that the velocity u is conserved in the axial direction. It is noted that anelastic numerical models of the solar dynamo, in which strong compression (but no variability in conductivity) is taken into account, have yielded some cases in which u is conserved on zonal flow cylinders, and other cases in which the flow velocity varies in the axial direction at depth (Brun and Toomre, 2002). In quasigeostrophic flows, viscous or turbulent shear tends to limit velocity gradients, favoring conservation of u on axial cylinders.

Previous investigations of the planetary dynamics can be broadly categorized as being of two types; shallow layer models, in which motion is restricted to the two horizontal dimensions on the spherical outer surface, and deep layer models, in which rapid rotation causes deep flows to be more or less two-dimensional, varying little in the direction of the rotation axis (quasigeostrophic approximation). Numerical shallow layer models have reproduced several generic features observed on Jupiter and Saturn, including multiple zonal jets of alternating direction, and strong equatorial flow (Williams, 1978; Cho and Polvani, 1996). However, in these models equatorial flow is retrograde (westward)—opposite in direction to the prograde (eastward) equatorial flow on Jupiter and Saturn. More recent shallow layer models have obtained prograde equatorial flow—but not without the application of ad hoc forcing functions (Williams, 2003). Indeed, the theory of geostrophic turbulence predicts retrograde zonal flow for a shallow 2D layer, depending on the sign of the shallow layer β-parameter (Yano et al., 2003, 2005).

In a pioneering study, Busse (1976) proposed that the jovian surface zonal flows could be a manifestation of deep convection. He suggested that the banded flow is an expression of deep geostrophic convection outside of the tangent cylinder (Fig. 2a). More recently, Christensen (2001, 2002) demonstrated that deep convection can produce jets of realistic amplitudes. However, his model produced only three jets outside the tangent cylinder and a pair of jets in each hemisphere inside the tangent cylinder, implying that deep rooted convection in a moderately thick fluid shell ($\chi = 0.60$) cannot account for the multiple high latitude jets of Jupiter and Saturn (Christensen, 2001).

Obtaining quasigeostrophic turbulence in fully 3D numerical models is computationally expensive. However, computational cost for rotating convection models can be substantially reduced by using a quasigeostrophic 2D approximation that takes into account spherical geometry and potential vorticity conservation (the topographic β-effect) while solving for flow in the equatorial plane. This 2D geostrophic approximation has been shown to agree qualitatively with results from laboratory experiments and 3D numerical models (Aubert et al., 2003), and can allow exploration of a greater range in parameter space (Gillet and Jones, 2006). Those models utilized a rigid (dissipative) outer boundary condition, which is applicable to flow in the Earth's core. However, the rigid outer boundary tends to inhibit jet formation, and those results are not clearly applicable to the giant planets, which lack a rigid outer surface.

Yano et al. (2003, 2005) constructed 2D non-convective geostrophic turbulence models with a free slip outer boundary and no inner boundary to approximate deep convection in a full sphere (without an inner boundary) and obtained results that resemble those of Christensen (2001).

Laboratory experiments of rotating convection in deep spherical shells necessarily feature rigid mechanical boundary conditions and replace central gravity with the rotation-driven centrifugal force. Nevertheless, using rapidly rotating spherical shell of radius ratios of $\chi = 0.35$ and 0.70, Manneville and Olson (1996) obtained zonal flow patterns that are broadly comparable to the results of spherical numerical models (Christensen, 2001; Aurnou and Olson, 2001). Multiple jets have been pro-

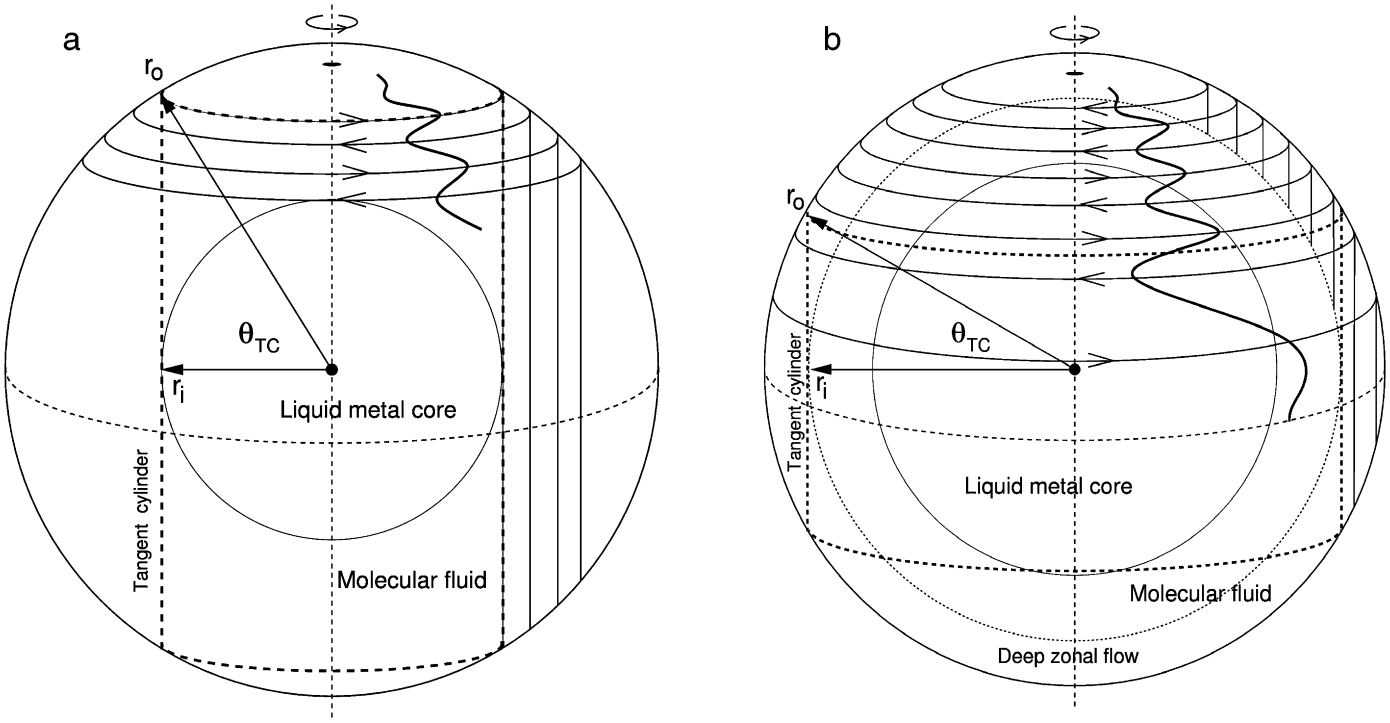

Fig. 2. Illustration of deep convection models. (a) In the model of Busse (1976) high latitude jets are the surface expression of deep flows that span the northern and southern hemispheres. Jets do not occur inside the tangent cylinder. (b) In the present model of deep turbulent convection in a relatively thin spherical shell, the tangent cylinder marks a discontinuity in the axial height of flow structures. Turbulent jets at high latitudes (inside the tangent cylinder) are underlain by flows that are effectively attenuated near the inner spherical boundary of radius r_i. Only the equatorial flows (outside the tangent cylinder) axially span the northern and southern hemispheres.

duced by idealized numerical (Jones et al., 2003) and experimental models with a cylindrical geometry, a free top surface, and a sloping, rigid bottom surface (Read et al., 2004). In those local models, as well as our present global model, the jets are produced by the topographic β-effect and follow Rhines scaling.

Several previous models of geostrophic or quasigeostrophic deep convection have explicitly or implicitly assumed that the high latitude jets observed on Jupiter and Saturn are the surface expression of flow structures outside the tangent cylinder (Busse, 1976; Sun et al., 1993; Yano et al., 2003, 2005). However, Christensen (2001) pointed out that the number alternating zonal bands increases with increasing radius ratio. Our model is based on the hypothesis that, while the equatorial jets of Jupiter and Saturn are underlain by deep flows outside the tangent cylinder, the higher latitude jets are underlain by bottom bounded zonal flows inside the tangent cylinder. In this model, quasigeostrophic, turbulent flow must develop inside the tangent cylinder in order for alternating high latitude jets to form. Fig. 2 illustrates these two different hypotheses for the deep source of surface zonal flows on Jupiter and Saturn.

This paper expands upon an earlier paper on the origin of Jupiter's high latitude jets (Heimpel et al., 2005), and is organized as follows. Numerical models of rotating convection are presented in Section 2. In Section 3 Rhines' scaling theory, which has previously been applied to deep geostrophic turbulence in a full sphere (Yano et al., 2003, 2005), is extended to a spherical shell geometry. In Sections 3, 4 and 5 spherical shell Rhines scaling is shown to be consistent with the zonal jet structures in our numerical model, as well as with those of Jupiter and Saturn. Lastly, in Section 6 we discuss implications of the spherical shell hypothesis. A list of symbols is given as Table 1.

2. Numerical modeling

Numerical simulations are employed to study thermal convection in spherical shells. A detailed description of the numerical model is given by Wicht (2002). The governing equations are

$$\frac{\partial \mathbf{u}}{\partial t} + \mathbf{u}\cdot\nabla\mathbf{u} + 2\,\hat{z}\times\mathbf{u} + \nabla P = E\nabla^2\mathbf{u} + Ra^*T\hat{r}, \tag{1}$$

$$\frac{\partial T}{\partial t} + \mathbf{u}\cdot\nabla T = EPr^{-1}\nabla^2 T, \tag{2}$$

$$\nabla\cdot\mathbf{u} = 0, \tag{3}$$

which are solved simultaneously to determine the fluid velocity vector $\mathbf{u}$ and the temperature field T.

The calculations are performed subject to a constant temperature difference, ΔT, that is maintained between isothermal, impermeable, mechanically stress free, inner and outer boundaries, r_i and r_o, respectively. Initial conditions are solid body rotation with angular velocity $\Omega\hat{z}$, and a small, random initial temperature perturbation, from which convection develops. Total angular momentum of the rotating, convecting system is conserved. The fluid is Boussinesq and its physical properties are characterized by α, the thermal expansion coefficient, ν, the kinematic viscosity, and κ, the thermal diffusivity.

Table 1
List of symbols

Notation	Description	Units
$C(\chi)$	Geostrophic jet scaling parameter	–[a]
$C^*(\theta_\chi)$	β-plane jet scaling parameter	–
D	Dimensionless spherical shell thickness	–
E	Ekman number	–
P	Dimensionless pressure	–
Pr	Prandtl number	–
Ra	Rayleigh number	–
Ra^*	Modified Rayleigh number	–
Re	Reynolds number	–
Ro	Rossby number	–
T	Dimensionless temperature	–
U	Scaling velocity	$\mathrm{m\,s^{-1}}$
f	Coriolis parameter	$\mathrm{s^{-1}}$
g	Gravitational acceleration	$\mathrm{m\,s^{-2}}$
h	Axial spherical shell height	m
$\mathbf{k}$	Wavevector	$\mathrm{m^{-1}}$
r_i	Inner spherical shell radius	m[b]
r_o	Planetary radius or outer spherical shell radius	m[b]
s	Cylindrical radial coordinate	m
u	Azimuthal velocity	$\mathrm{m\,s^{-1}}$
$\mathbf{u}$	Dimensionless velocity vector	–
β	Vorticity gradient parameter	$\mathrm{m^{-1}\,s^{-1}}$
χ	Ratio of inner & outer spherical boundaries	–
Ω	Planetary rotation rate	$\mathrm{s^{-1}}$
κ	Thermal diffusivity	$\mathrm{m^2\,s^{-1}}$
$\lambda, \lambda/2$	Jet wavelength & jet width	rad
$\lambda_J/2$	Measured jet width	rad
λ_g	Geostrophic Rhines wavelength	rad
λ_β	β-plane Rhines wavelength	rad
ν	Kinematic viscosity	$\mathrm{m^2\,s^{-1}}$
θ	Latitude	rad
θ_{TC}	Latitude at intersection of tangent cylinder with outer boundary	rad
$\xi, \xi(\theta)$	Jet scaling parameter & function	–

[a] Dimensionless.
[b] Or dimensionless, depending on context.

Equations (1)–(3) have been non-dimensionalized using the spherical shell thickness $D = r_o - r_i$ for length, Ω^{-1} for time, ΩD for velocity, $\rho\Omega^2 D^2$ for pressure and ΔT for temperature. The controlling non-dimensional parameters for this system are: the Ekman number, $E = \nu/(\Omega D^2)$, which is the ratio of the viscous to Coriolis forces; the Prandtl number, $Pr = \nu/\kappa$, which is the ratio of the viscous and the thermal diffusivities of the working fluid; and the modified Rayleigh number $Ra^* = \alpha g \Delta T/(\Omega^2 D)$, which is the ratio of buoyancy to the Coriolis force, where g is the gravitational acceleration on the outer boundary. The modified Rayleigh number may be written in terms of the conventional Rayleigh number $Ra = \alpha g \Delta T D^3/(\kappa\nu)$, as $Ra^* = RaE^2/Pr$ (Christensen, 2002). It should also be noted that $\sqrt{Ra^*}$ is known as the convective Rossby number (e.g., Vorobieff and Ecke, 2002). In the calculations presented here, the Ekman number is $E = 3 \times 10^{-6}$, the Prandtl number is $Pr = 0.1$, and the modified Rayleigh number is $Ra^* = 0.05$.

The spherical shell geometry is defined by the radius ratio $\chi = r_i/r_o$, where r_i is the inner boundary radius and r_o is the outer boundary radius. Simulations are performed for two values of the radius ratio; $\chi = 0.85$ and $\chi = 0.9$ (see Fig. 2). The shells with $\chi = 0.85$ and $\chi = 0.9$ are substantially thinner than in previous models of rotating convection that have been applied to the zonal winds of Jupiter and Saturn (Aurnou and Olson, 2001; Christensen, 2001, 2002; Aurnou and Heimpel, 2004). The radius ratio $\chi = 0.9$ lies roughly in the middle of current estimates for the depth of fast zonal flow in Jupiter (Guillot et al., 2004).

The pseudo-spectral numerical code was originally developed to model the solar dynamo (Glatzmaier, 1984) and has been since modified (Glatzmaier and Roberts, 1995; Christensen et al., 1999; Wicht, 2002). The code implemented here has been benchmarked and uses mixed implicit/explicit time stepping (Wicht, 2002). To save computational resources, the governing equations are solved on azimuthally truncated spheres with eight-fold symmetry (Al-Shamali et al., 2004), with periodic boundary conditions on the bounding meridional planes. Each of the numerical grids for the two different radius ratios ($\chi = 0.85$ and $\chi = 0.9$) has 65 radial grid-points. For the $\chi = 0.85$ case the spherical section has 512 points in latitude and 128 points in longitude. The $\chi = 0.9$ case has 768 points in latitude and 192 longitudinal points on the truncated section. The imposed eight-fold symmetry can make the solutions

Table 2
Definitions and values of the numerical model's non-dimensional control parameters (χ, E, Ra, Pr) and output parameters (Re, Ro), along with estimates of those parameters for Jupiter and Saturn

Parameter	Numerical model	Jupiter	Saturn
$\chi = r_i/r_o$	0.85 & 0.9	0.80–0.95	0.50–0.85
$E = \nu/\Omega r_o^2(1-\chi)^2$	3×10^{-6}	10^{-15}–10^{-20}	10^{-15}–10^{-20}
$Ra = \alpha g_o \Delta T r_o^3(1-\chi)^3/\kappa\nu$	5.56×10^8	10^{25}–10^{30}	10^{25}–10^{30}
$Pr = \nu/\kappa$	0.1	~0.1	~0.1
$Re = U(r_o - r_i)/\nu$	5×10^4	10^{15}	2×10^{15}
$Ro = U/(\Omega r_o)$	0.012–0.025	0.01	0.04

Notes. The Reynolds and Rossby numbers given here are based upon the approximate peak zonal flow velocities. It is noted the numerical model with $\chi = 0.9$ was previously presented in Heimpel et al. (2005). In that paper, Ra was given, in error, as 1.67×10^{10}. The value given here is correct for this paper and for the previous work.

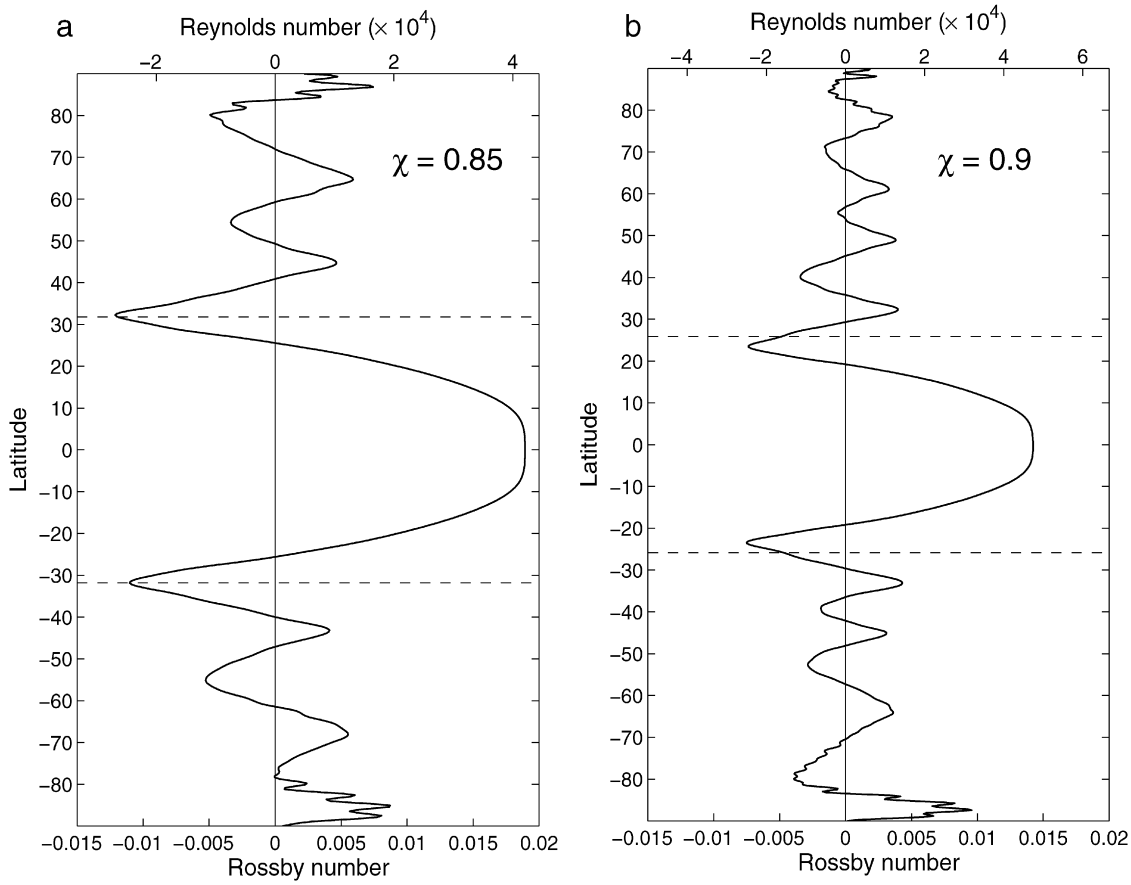

Fig. 3. Results from numerical models with $Ra^* = 0.05$, $E = 3 \times 10^{-6}$ and $Pr = 0.1$. Outer surface azimuthally-averaged azimuthal flow velocity profiles for two different values of the radius ratio $\chi = r_i/r_o$. (a) $\chi = 0.85$; (b) $\chi = 0.9$. The dashed lines show the latitude θ_{TC} at which the tangent cylinder intersects the outer surface. Both velocity profiles are averaged in time over about 100 rotations. The flow velocities are scaled by the Rossby number $Ro = u/(\Omega r_o)$ (bottom axis) and the Reynolds number $Re = uD/\nu = Ro/[E(1-\chi)]$ (top axis).

more axially symmetric. However, the simulations are characterized by strong rotation and vigorous convection, such that the flow has strong cylindrical symmetry and several plume structures occur in the equatorial region of a truncated section (see Fig. 4d). This indicates that the eight-fold truncation should not have a strong effect on the solution.

The use of hyperdiffusion allows us to resolve these models with relatively high Ra and low E. A potential pitfall of using hyperdiffusion is that it may introduce anisotropy between radial and azimuthal modes of flow. In addition, hyperdiffusivity yields a viscosity that increases with decreasing scale so that, on average, the effective Rayleigh number decreases and the effective Ekman number increases with the strength of hyperdiffusion. However, we have used relatively weak hyperdiffusion which seems to act mainly as a low-pass filter. Thus the medium and long wavelength structure that we are interested in (the azimuthal jets) seem not to be significantly affected. Runs were calculated with hyperdiffusivity of the same functional form as previous dynamo models (Stanley and Bloxham, 2004; Kuang and Bloxham, 1999). For the $\chi = 0.9$ case, the initial hyperdiffusion amplitude was reduced as the calculation became steadier in time. The final amplitude of the hyperdiffu-

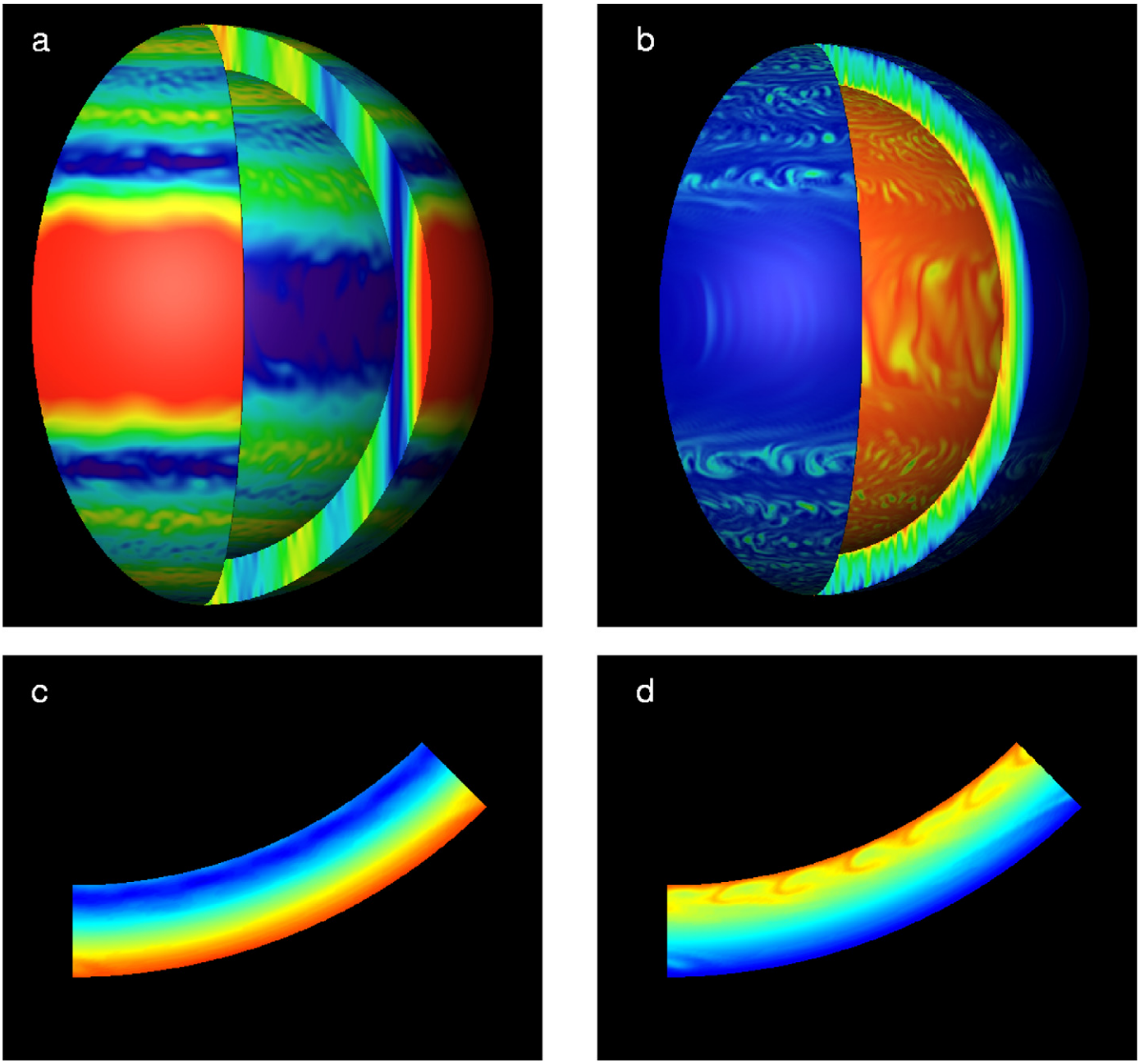

Fig. 4. Results from $\chi = 0.85$ numerical simulation. (a and c) Snapshot of the azimuthal velocity field. Red and blue represent prograde (eastward) and retrograde (westward) flow, respectively. In (a) the velocity field is displayed on the inner and outer spherical surface, and on a meridional slice, which shows the columnar (quasigeostrophic) structure of the flow field. In (c) a latitudinal slice (at 10° latitude) of the azimuthal velocity field is displayed. (b and d) Snapshot of temperature field. Red and blue represent cold and warm temperatures, respectively. In (d) the latitudinal slice reveals six individual hot plume structures. (For interpretation of the references to color in this figure ledend, the reader is referred to the web version of this article.)

sivity was smaller than that of the previous dynamo models by 1/10 (Kuang and Bloxham, 1999). Similarly, the Ekman number was lowered in stages. After E was reduced from 3×10^{-5} to 3×10^{-6} the model was run for over 1600 planetary rotations and the convective motions approached a statistically-steady state. For the case of $\chi = 0.85$, the hyperdiffusion and Ekman number were constant throughout the calculation and equal to the final values of the $\chi = 0.9$ case.

The model parameters were selected to reflect (within technical limitations) our current understanding of the jovian and saturnian dynamics. Table 2 summarizes our parameter choices as well as estimates of relevant parameters for Jupiter and Saturn. The model values of Ra^* and E are based on recent numerical and experimental scaling analyses for convection driven zonal flows in thicker spherical shells (Aubert et al., 2001; Christensen, 2002). The Ekman number was chosen to be as low as is technically feasible. Then, Ra^* was chosen to obtain an a zonal flow with velocity (or Rossby number Ro) that approximates the jovian planets. Thus, while Ra and E^{-1} for our simulations are several orders of magnitude less than planetary

values, the simulation values of *Ro* are representative of the giant planets.

An essential ingredient in our numerical simulations is that the convection drives the system to fully developed inertial turbulence that is quasigeostrophic and close to the asymptotic regime of rapid rotation, where viscosity and thermal diffusivity play a negligible role in the dynamics. The existence of such a regime is supported by the asymptotic scaling relationships of Christensen (2002). Thus, the large discrepancies between the simulation parameters and those estimated for Jupiter may not strongly affect the character of the solution.

We do not model the jovian troposphere nor the effects of latitudinally varying insolation (Williams, 1978, 2003). Furthermore, we model convection only within the region where large-scale zonal flows are predicted to occur and we neglect the deeper regions where convection may be vigorous but zonal flows are expected to be weak. Although density increases by several orders of magnitude with depth below Jupiter's troposphere, our model neglects fluid compression (Boussinesq approximation). This is clearly a drastic simplification since fluid compressibility effects are certainly important to the dynamics of convection in the Gas Giants (Evonuk and Glatzmaier, 2004; Glatzmaier, 2005a). While the Boussinesq model is inadequate to describe convection within the Gas Giants, it can provide insight into the large-scale dynamics (Yano et al., 2003, 2005). The relevance and shortcomings of Boussinesq models can be qualitatively appreciated by comparing them with models that include density changes through the anelastic approximation. Such models, which have been applied to Saturn (Glatzmaier, 2005b), and solar convection (e.g., Brun and Toomre, 2002), typically produce quasigeostrophic, counter-rotating, cylindrical flows, with deep velocity fields that are comparable to Boussinesq flows.

Surface zonal flow profiles for the two calculations ($\chi = 0.85$, and $\chi = 0.9$ with $E = 3 \times 10^{-6}$), which are plotted in Fig. 3, show that the number of high latitude jets increases in proportion to the radius ratio χ. It is apparent from Fig. 3 that the thinner shell results in lower Rossby number (which scales the zonal flow velocity) and a smaller latitudinal wave length of zonal flow undulations inside and outside the tangent cylinder. Thus thinner shells favor the formation of multiple high latitude jets not only because the range of latitudes inside the tangent cylinder increases with χ, but also because the zonal jet wave length scales with velocity. Turbulent flow is essential for the development of multiple jets at higher latitudes, inside the tangent cylinder. The Reynolds number $Re = uD/\nu$ for our simulations (shown along with *Ro* in Fig. 3) has peak values of 10,000–15,000 and 40,000–47,000 inside and outside the tangent cylinder, respectively. These values of *Re* are sufficiently high at all latitudes for the development of strong inertial turbulence.

Fig. 4 shows the zonal flow field and the thermal field for the case with $\chi = 0.85$. Both images show strongly anisotropic flow structures associated with rapid rotation. The flow and thermal fields vary little in the axial direction, and turbulent flow structures are suppressed on planes parallel to the rotation axis. (Note that turbulent flow is apparent on all surfaces except the meridional planes, where they appear to be strongly aligned with the axial direction.) Furthermore Fig. 4a shows that the zonal flow is strongly columnar throughout the fluid, with nested cylindrical flows of alternating direction outside and inside the tangent cylinder (as shown schematically in Fig. 2b).

3. Scaling of turbulent planetary zonal flow

3.1. Rhines wavelength for the β-plane approximation

Energy in turbulent flow typically passes from larger to smaller scales. However, the interaction of two-dimensional turbulence with the combined effect of planetary rotation and spherical boundary curvature can give rise to an energy transfer from smaller eddies to larger, zonally extended eddies (Rhines, 1975). In the β-plane approximation (which assumes that planetary flows are shallow, such that radial motion is neglected) this inverse cascade ceases approximately at a wavenumber

$$k_\beta = \sqrt{\beta/2U}, \tag{4}$$

where U is a velocity scale and $\beta = (1/r_o)\,\mathrm{d}f/\mathrm{d}\theta$ is the gradient of the Coriolis parameter ($f = 2\Omega\sin\theta$) on a 2D spherical surface of radius r_o that rotates with angular velocity Ω, and θ is the latitude ($-\pi/2 \leqslant \theta \leqslant \pi/2$). Equation (4) is Rhines (1975) original expression. In the subsequent literature, to emphasize the approximate nature of the expression, the factor of 2 in the denominator has often been omitted, and the length scale $L_\beta \simeq \pi/k_\beta$ is known as Rhines scale (Vasavada and Showman, 2005). Here, we choose to retain the factor of 2 and write, for the β-plane approximation, the angular form of Rhines wavelength (given in radians) as

$$\lambda_\beta = \frac{2\pi}{r_o k_\beta} = 2\pi\sqrt{\frac{U}{r_o\Omega\cos\theta}}, \tag{5}$$

which is expected to characterize the latitudinal scale of zonal jets.

3.2. Rhines wavelength for a spherical shell

For approximately geostrophic flow in a rapidly rotating 3D spherical shell, zonally extended eddies evolve into jets of alternating prograde and retrograde velocity, which obtain the form of nested cylinders aligned with the rotation axis. This system can be thought of as a fluid layer in which the depth h is measured in the axial direction (Fig. 5), with a constant Coriolis parameter $f = 2\Omega$. It follows that the Rhines length can be formulated in terms of the topographic β-parameter, $\beta = -2\Omega(\mathrm{d}h/\mathrm{d}s)/h$ (Pedlosky, 1979; Yano et al., 2005). Due to geostrophy the velocity structure has cylindrical symmetry and varies dominantly in the direction normal to the rotation axis. Thus, the generalization of Rhines scaling for flow in a 3D spherical shell is represented by the wavevector $\mathbf{k} = \sqrt{|\beta|/2U}\,\hat{\mathbf{s}}$, where $\hat{\mathbf{s}} = \hat{\mathbf{r}}\cos\theta + \hat{\boldsymbol{\theta}}\sin\theta$ is the cylindrical radius unit vector, decomposed into latitudinal and radial component vectors. We note that the absolute value of β appears here since

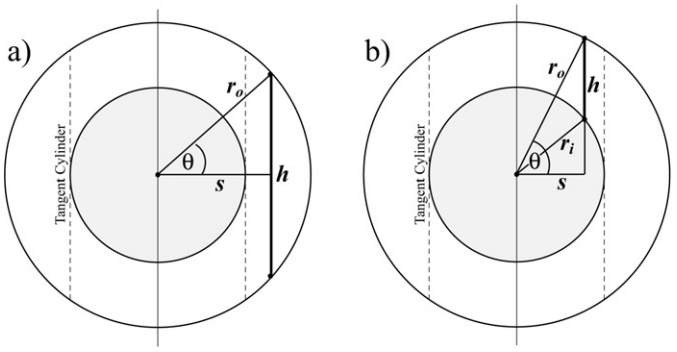

Fig. 5. Schematics illustrating (a) height, h, of a fluid column located in the equatorial region outside the tangent cylinder (i.e., at latitudes $\theta \leqslant \theta_{\rm TC}$); (b) height of a fluid column in the high latitude region located inside the tangent cylinder (i.e., at latitudes $\theta \geqslant \theta_{\rm TC}$). The radii of the outer and inner boundaries are, respectively, r_i and r_o, and the cylindrical radius is s.

β changes sign for a deep spherical shell. For planetary observations, we are interested in the magnitude of $\mathbf{k}$ in the θ direction, so the Rhines wavenumber on the spherical outer boundary becomes $k = \sin\theta\sqrt{|\beta|/2U}$. Thus, for the geostrophic approximation, the Rhines wavelength on the outer spherical surface is

$$\lambda_{\rm g} = \frac{2\pi}{r_o}\frac{1}{k} = \frac{2\pi}{r_o \sin\theta}\sqrt{\frac{U h}{\Omega\,|{\rm d}h/{\rm d}s|}}. \tag{6}$$

By evaluating h for the spherical shell geometry, we can proceed to obtain the Rhines wavelength as a function of latitude. Fig. 5 illustrates the relevant geometric features for a spherical shell of inner radius r_i and outer radius r_o. For rapidly rotating systems, the tangent cylinder represents a boundary that separates planetary flows into three relatively independent volumetric regions (Aurnou et al., 2003); the equatorial region outside the tangent cylinder, the northern region inside the tangent cylinder, and the southern region inside the tangent cylinder. Here it is significant that, for a spherical shell of radius ratio $\chi = r_i/r_o$, the value of h doubles discontinuously while ${\rm d}h/{\rm d}s$ changes sign equatorward across the latitude $\theta_{\rm TC} = \cos^{-1}\chi$, which represents the intersection of the tangent cylinder with the outer surface. Axially aligned flow structures of height h may be considered to correspond to Taylor columns (Schoff and Colin de Verdiere, 1997). For Boussinesq or adiabatically mixed (Ingersoll and Pollard, 1982), fully developed, quasi-geostrophic turbulence, large-scale flow structures tend to be cylindrical and are aligned with the planetary rotation axis.

Fig. 5a shows the geometry in the region outside the tangent cylinder ($s \geqslant r_i$). The height of an axial fluid column is

$$h = 2\left(r_o^2 - s^2\right)^{1/2}. \tag{7}$$

The variation of column height with cylindrical radius is

$$\frac{1}{h}\left|\frac{{\rm d}h}{{\rm d}s}\right| = \frac{s}{r_o^2 - s^2} = \frac{1}{r_o}\left(\frac{\cos\theta}{\sin^2\theta}\right). \tag{8}$$

Outside the tangent cylinder, the Rhines length in radians on the outer spherical surface is

$$\lambda_{\rm g} = 2\pi\sqrt{\frac{U}{r_o\Omega\cos\theta}}; \quad |\theta| \leqslant \cos^{-1}\chi. \tag{9}$$

Comparing (5) and (9) shows that the Rhines wavelength for the β-plane approximation is identical to that of the equatorial region outside the tangent cylinder for the geostrophic approximation. Furthermore, the geostrophic Rhines length for a full sphere geometry ($\chi \to 0$), in which all the fluid is effectively outside of the tangent cylinder ($\theta_{\rm TC} \to \pm 90°$ latitude), has the same formulation, at all latitudes, as the β-plane Rhines length.

Fig. 5b shows the geometry of an axial fluid column of height h located inside the tangent cylinder ($s \leqslant r_i$). The column height is

$$h = \left(r_o^2 - s^2\right)^{1/2} - \left(r_i^2 - s^2\right)^{1/2}. \tag{10}$$

Following the same procedure as above, it is found that

$$\frac{1}{h}\frac{{\rm d}h}{{\rm d}s} = \frac{s}{(r_o^2 - s^2)^{1/2}(r_i^2 - s^2)^{1/2}} \tag{11}$$

which can be cast into the form

$$\frac{1}{h}\left|\frac{{\rm d}h}{{\rm d}s}\right| = \frac{1}{r_o}\left|\frac{\cot\theta}{\sqrt{\chi^2 - \cos^2\theta}}\right|. \tag{12}$$

Combining (12) and (6), the Rhines wavelength in radians on the outer sphere becomes

$$\lambda_{\rm g} = 2\pi\sqrt{\frac{U}{r_o\Omega}\left|\frac{(\chi^2 - \cos^2\theta)^{1/2}}{\sin\theta\cos\theta}\right|}; \quad |\theta| \geqslant \cos^{-1}\chi. \tag{13}$$

We note that in the limiting case of an arbitrarily thin shell, $\chi = 1$, Eq. (13) reduces again to (5) and (9). Thus the three limiting cases of a 2D shallow layer (β-plane approximation), a 3D deep layer (geostrophic approximation) with $\chi = 0$ and a 3D shallow layer with $\chi \to 1$ all have identical Rhines scaling. However, this analysis only pertains to the characteristic length-scale of the zonal flows; the flow *directions* of individual zonal jets need not be the same (Yano et al., 2005).

3.3. Comparison of Rhines scale and measured jet widths

Using (9) and (13) we may test the applicability of Rhines scaling to our numerical results and to the giant planets. Using the surface wind profile provided by A. Vasavada (see Fig. 1) we measure Jupiter's jet widths. Similarly we measure the jet widths for the surface flow fields of our two numerical simulations (with radius ratios $\chi = 0.85$ and $\chi = 0.9$). We did not quantitatively consider Saturn's jet widths since the present uncertainty in the planetary rotation rate (Sanchez-Lavega, 2005) complicates the measurement.

The jet width, defined here to be equal to half a wavelength $\lambda/2$ of latitudinal velocity variations, is measured as the latitudinal distance between minima in $|u|$, where u is the azimuthally averaged zonal surface flow velocity for Jupiter or the numerical model. From this definition of jet width it follows that a jet boundary can occur where u crosses zero, or where u is finite but $|u|$ is a minimum. The graphical basis for measurement is shown in Fig. 6.

To obtain jet widths predicted by Rhines scaling we calculate the mean values for the right-hand side of (9) and (13), where

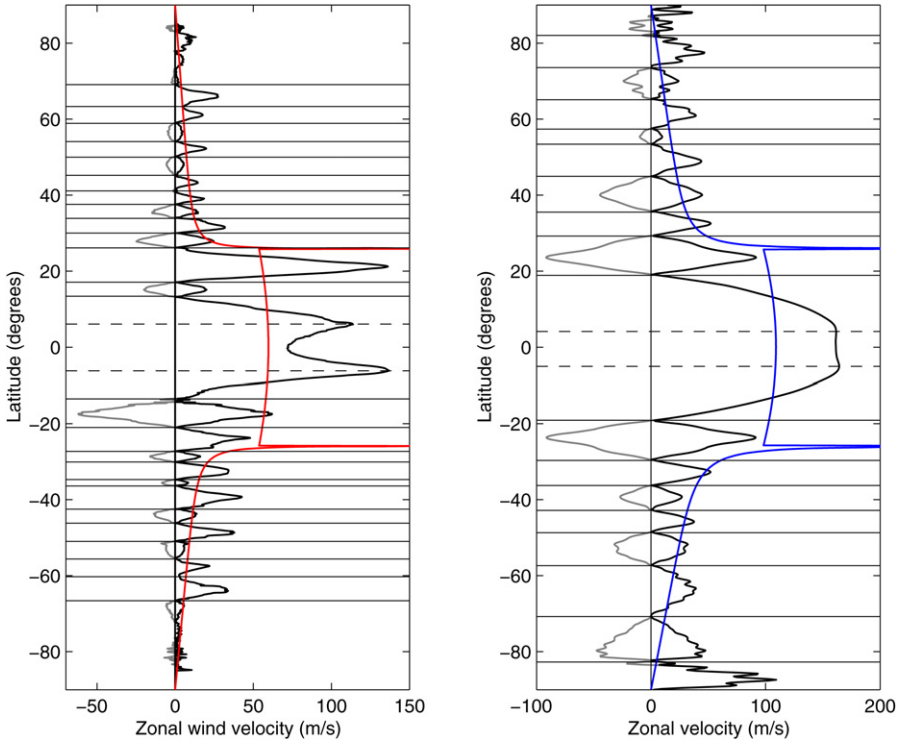

Fig. 6. Velocities and jet boundaries for (a) Jupiter and (b) the numerical model. It is noted that the horizontal scale is different in (a) and (b). Observed profiles of the absolute value of the surface velocity $|u|$ are shown as black curves. The actual velocity profiles (showing the retrograde jets in gray) are plotted for reference. The jet boundaries are plotted as light solid lines of latitude. The dashed lines of latitude are at the peaks of the jets nearest the equator. The jet width associated with those peaks is twice the latitude distance from the dashed line to the next jet boundary at higher latitude. The scaling velocity $U(\theta)$ (red for Jupiter and blue for the numerical model) is calculated from (23), which is based on the assumption of constant Rhines length in each of the three regions; north, south and equatorial. (For interpretation of the references to color in this figure ledend, the reader is referred to the web version of this article.)

the velocity scale U is taken to be $\langle |u| \rangle_J$, which represents latitudinal mean of the azimuthally averaged zonal surface velocity for each jet.

Figs. 7–10 show the applicability of Rhines scaling to the zonal flow on Jupiter and for our numerical simulations. Fig. 7 compares the observed and simulated jet widths against the jet widths predicted by Rhines scaling. For the simulations, the correspondence between measured and predicted jet widths is seen to be close outside the tangent cylinder, although, for the $\chi = 0.9$ case the highest latitude simulated jets are significantly narrower than predicted by Rhines scaling. For both the $\chi = 0.85$ and $\chi = 0.9$ cases the simulated equatorial jets are much broader than predicted. For Jupiter the predicted jet width values are calculated using $\chi = 0.9$ in (9) and (13). Although there is clearly some misfit between the measured and predicted jet widths, it is remarkable that Jupiter's measured jet widths correspond well to the values calculated using Rhines scaling, except at the highest latitudes, where, similar to the simulated cases, Rhines scaling overestimates the jet widths.

Fig. 8 shows the measured jet widths for Jupiter against the predicted jet widths for several values of the radius ratio χ. Fig. 9 shows the magnitude of the difference between the measured and predicted jovian jet widths (the misfit) with the same set of χ—values as in Fig. 7. These two figures show that, while it is plausible to fit Jupiter's jet widths with those predicted by Rhines scaling for any spherical shell layer depth (or radius ratio χ), the best fits occur for radius ratios between about 0.85 and 0.95. This is graphically quantified in Fig. 10, which shows the misfit between measured and predicted values, averaged over all measured jovian jets, as a function of χ. Here we see that, compared to what Rhines scaling predicts for full sphere ($\chi = 0$) or an extremely shallow layer ($\chi \simeq 1$) the minimum misfit (at $\chi = 0.86$) is improved by roughly 33%.

3.4. A geometrical jet scaling function

The geostrophic Rhines wavelength, in radians of latitude on the surface of a rapidly rotating spherical shell, is specified by (9) and (13) outside and inside the tangent cylinder, respectively. In this formulation λ_g depends on the spherical geometry, the velocity scale U, the angular rotation rate Ω and the characteristic length-scales of the system, r_o and D. We may isolate the purely geometrical part of the Rhines scaling relationship by writing

$$\xi = \frac{\lambda_g}{2\pi}\sqrt{\frac{r_o \Omega}{U}} \tag{14}$$

which we refer to as the *jet scaling parameter*. Combining (9), (13) and (14) we see that, outside the tangent cylinder,

$$\xi(\theta) = \sqrt{\frac{1}{\cos\theta}}; \quad |\theta| \leqslant \cos^{-1}\chi, \tag{15}$$

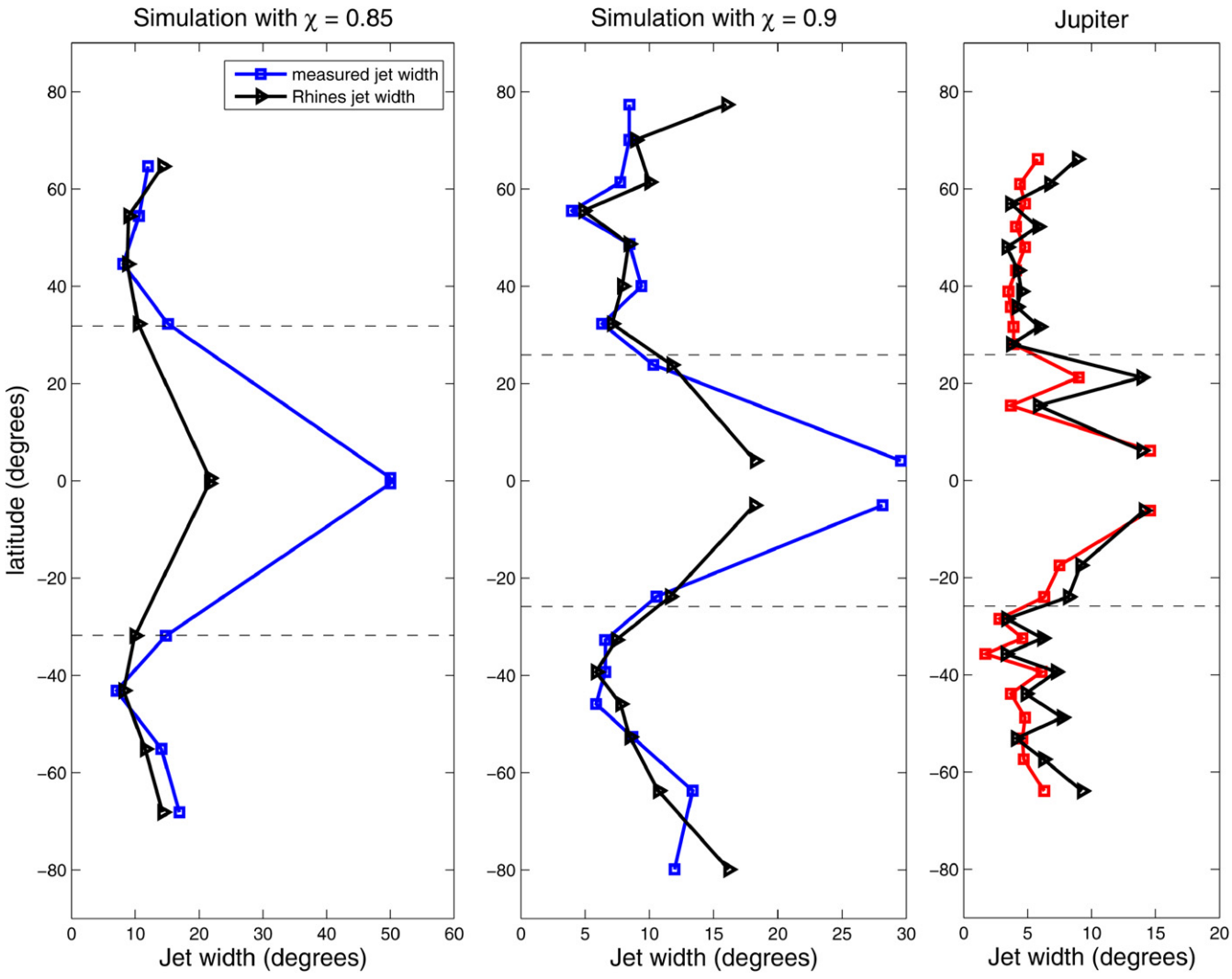

Fig. 7. Comparison of measured and predicted jet widths for two numerical simulations (with radius ratios $\chi = 0.85$ and $\chi = 0.9$), and for Jupiter, where the predicted values are obtained by assuming $\chi = 0.9$. The predicted values are obtained from (9) and (13), which are derived from Rhines scaling theory for turbulent flow in spherical shells of radius ratio χ. The method of jet measurement is shown in Fig. 6.

and inside the tangent cylinder,

$$\xi(\theta) = \sqrt{\left|\frac{(\chi^2 - \cos^2\theta)^{1/2}}{\sin\theta\cos\theta}\right|}; \quad |\theta| \geqslant \cos^{-1}\chi. \tag{16}$$

The functional form of the jet scaling parameter $\xi(\theta)$, given by (15) and (16), will be referred to as the *jet scaling function*, and is plotted for several values of χ in Fig. 11. It should be noted that Eq. (15), which is valid outside the tangent cylinder, is independent of χ.

4. Jet scaling for the numerical model and Jupiter

4.1. Rhines scale for each jet

Here we compare the jet scaling function $\xi(\theta)$, given by (15) and (16), to the *observed* or *measured* values of the jet scaling parameter ξ, given by (14), so that for each jet

$$\xi_J = \frac{\lambda_J}{2\pi}\sqrt{\frac{r_o\Omega}{\langle|u|\rangle_J}}. \tag{17}$$

Equation (17) has the same form as (14), but with the Rhines wavelength λ_g replaced by the measured jet wavelength, λ_J, and the velocity scale U replaced by the latitudinally and azimuthally averaged jet velocity $\langle|u|\rangle_J$, which was introduced in Section 3.3.

In Fig. 12, $\xi(\theta)$ given by (15) and (16) with $\chi = 0.9$ is plotted against the measured ξ_J values, for the numerical model and Jupiter, using the mean velocity $\langle|u|\rangle_J$ and measured width $\lambda_J/2$ for each jet. In addition $\xi = \sqrt{1/\cos\theta}$, which represents $\chi = 0$, $\chi \to 1$, and the β-plane approximation, is plotted for reference.

4.2. Global and regional jet scaling

In Section 3.3 we directly compared measured jet widths with those predicted by Rhines scaling. To eliminate the dependence of the jet width on the local velocity U we use, in Section 4.1, the jet scaling function $\xi(\theta)$ to compare observed to predicted jet scaling. Since $\xi(\theta)$ is purely geometrical (depending only on the latitude), no assumptions are re-

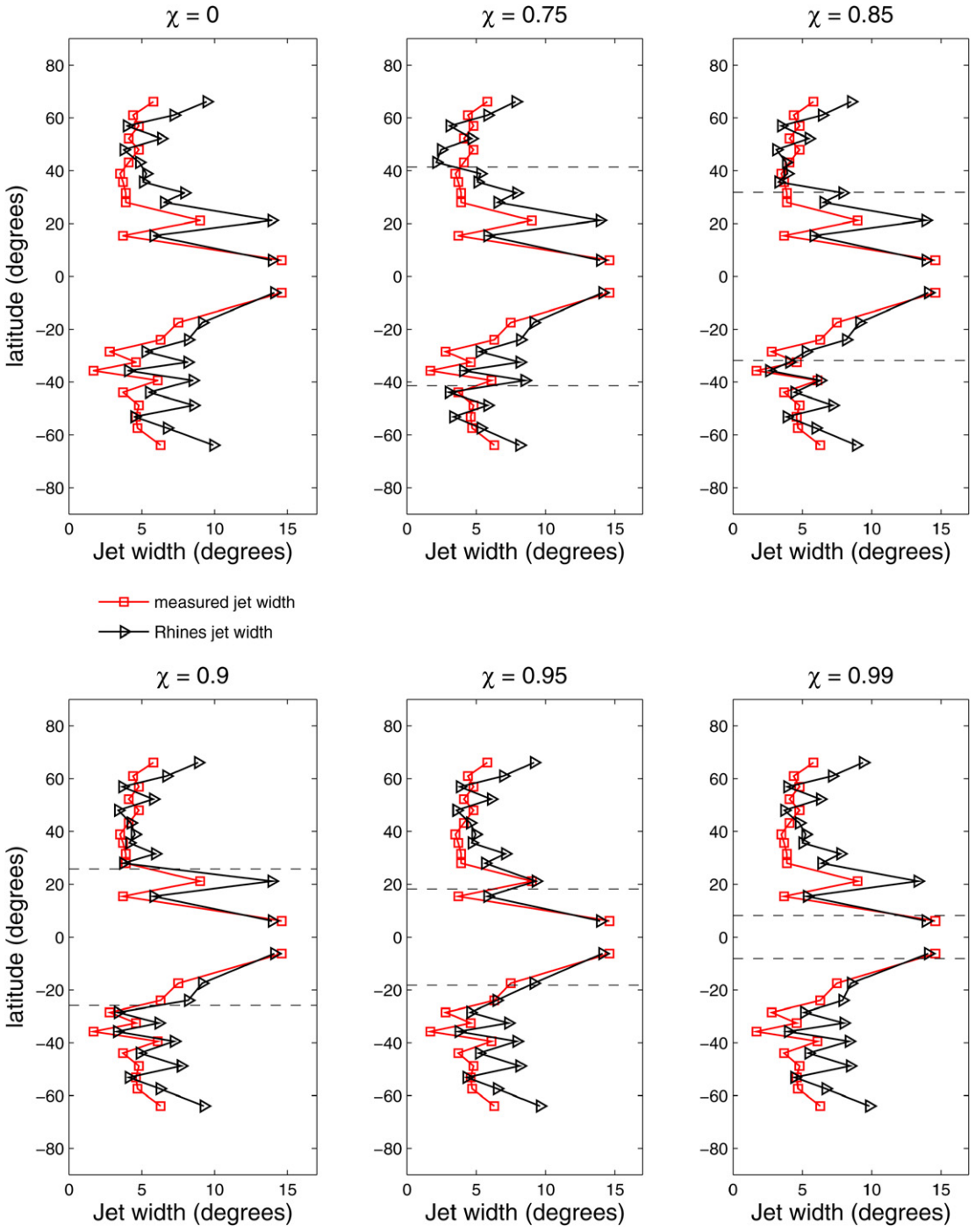

Fig. 8. Measured and predicted values of Jupiter's jet widths for several values of the radius ratio χ. See text and Fig. 7 caption for explanation of predicted values.

quired about the latitudinal relationship between λ_g and U. However, inspection of the zonal velocity profiles of Jupiter and Saturn shows that, outside the equatorial region, the latitudinal jet wavelength is approximately constant. This suggests a different approach in which λ_g is set to be constant over some range of latitudes, which implies a latitudinally variable velocity scale U. Furthermore, latitudinal variation of the velocity scale seems appropriate since quasigeostrophic flow is strongly anisotropic with weak, scale dependent mixing in latitude (Yano et al., 2005). Thus, we interpret $U(\theta)$ to be an azimuthally averaged velocity scale that may vary in latitude θ.

In a rapidly rotating spherical shell geostrophy inhibits flow across the inner shell tangent cylinder. This suggests that zonal flow scaling be analyzed separately inside and outside the tangent cylinder. Following this line of reasoning, we will, in this section, assume that the Rhines length is constant in each of the three regions bounded by the tangent cylinder: (1) the northern region, inside the tangent cylinder; (2) the southern region inside the tangent cylinder; (3) and the equatorial region, out-

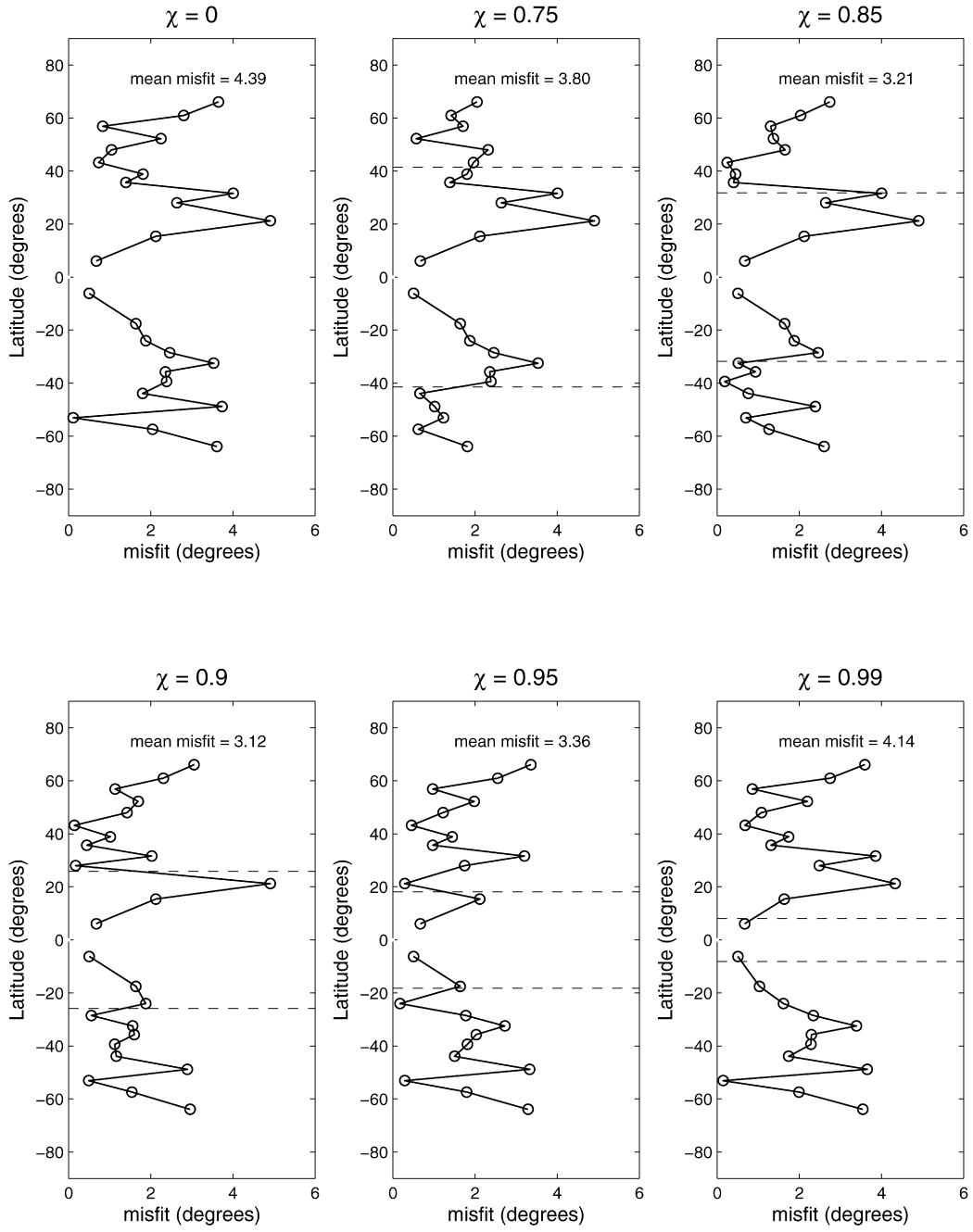

Fig. 9. Misfit (i.e., magnitude of the difference) between predicted and measured values of Jupter's jet widths for several values of the radius ratio χ (see Fig. 8).

side the tangent cylinder. We shall see that the assumption of regionally constant Rhines length seems to be well justified by the results.

With the Rhines wavelength λ_g taken to be regionally constant (but as yet undetermined), the scaling velocity is now a function of latitude. Thus Eq. (14) implies

$$U(\theta) = \frac{r_o \Omega \lambda_g^2}{4\pi^2} \frac{1}{\xi^2(\theta)}. \tag{18}$$

The latitude dependence of $U(\theta)$ is given by $1/\xi^2(\theta)$, which is singular on the inside part of the tangent cylinder boundary [see Eq. (16)]. This singularity may be thought of as being due to discontinuous vortex stretching implied by the two-fold jump in fluid column height h across the tangent cylinder.

With λ_g assumed to be constant for each of the three regions, northern, southern, and equatorial (or over any latitudinal region of interest), we take the regional latitudinal mean of both sides of (18):

$$\langle U \rangle = \frac{r_o \Omega \lambda_g^2}{4\pi^2} \left\langle \frac{1}{\xi^2(\theta)} \right\rangle. \tag{19}$$

Now, solving for λ_g yields an expression that allows us to calculate the Rhines wavelength based upon a regional, latitudinally

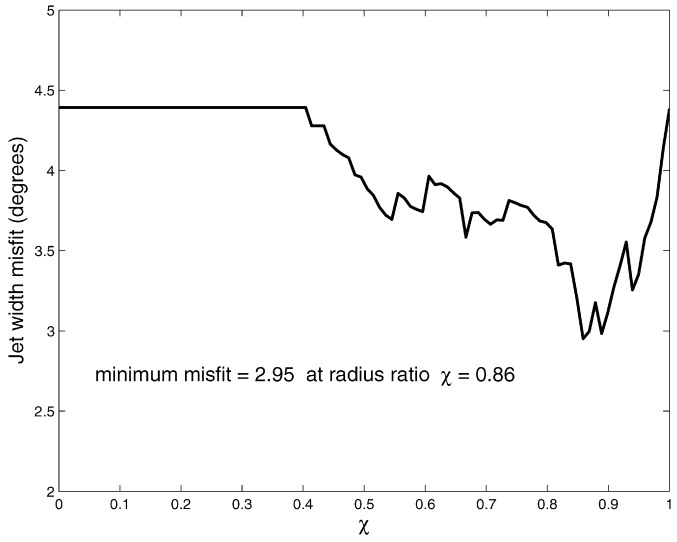

Fig. 10. Mean jet misfit for Jupiter (see Fig. 9) as a function of the radius ratio χ. The minimum misfit at $\chi = 0.86$ corresponds to the best estimate of the depth of fast zonal flow in Jupiter, according to Rhines scaling theory applied to a spherical shell of Boussinesq fluid. It is noted that the misfit is flat for $\chi \lesssim 0.4$ since the highest latitude measured jet is at $\cos^{-1}(0.4) = 66°$.

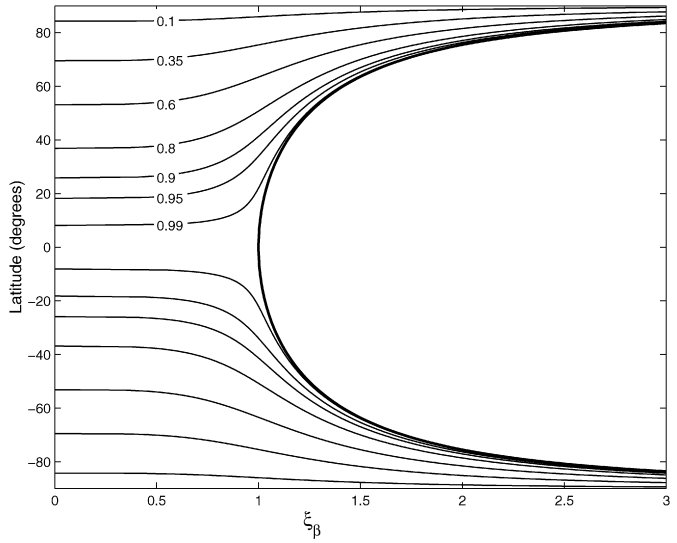

Fig. 11. The function $\xi(\theta)$ for a spherical shell, plotted for several values of the radius ratio $\chi = r_i/r_o$. Curves inside the tangent cylinder are calculated from (16) and labeled with χ-values in the northern hemisphere. The heavier solid curve, calculated from (15), is valid outside the tangent cylinder for all χ-values, as well as for the shallow layer (β-plane) approximation.

averaged azimuthal velocity profile $\langle U \rangle$,

$$\lambda_g = 2\pi \sqrt{\frac{\langle U \rangle}{r_o \Omega\, C(\chi)}}, \tag{20}$$

where we have defined the purely geometrical parameter $C(\chi) \equiv \langle 1/\xi^2(\theta) \rangle$, with the mean taken over the latitudinal region of interest. We note that, although $1/\xi^2(\theta)$ (and thus $U(\theta)$) is singular on the inside boundary of the tangent cylinder, $C(\chi)$ is finite, as can be seen by computing the mean inside

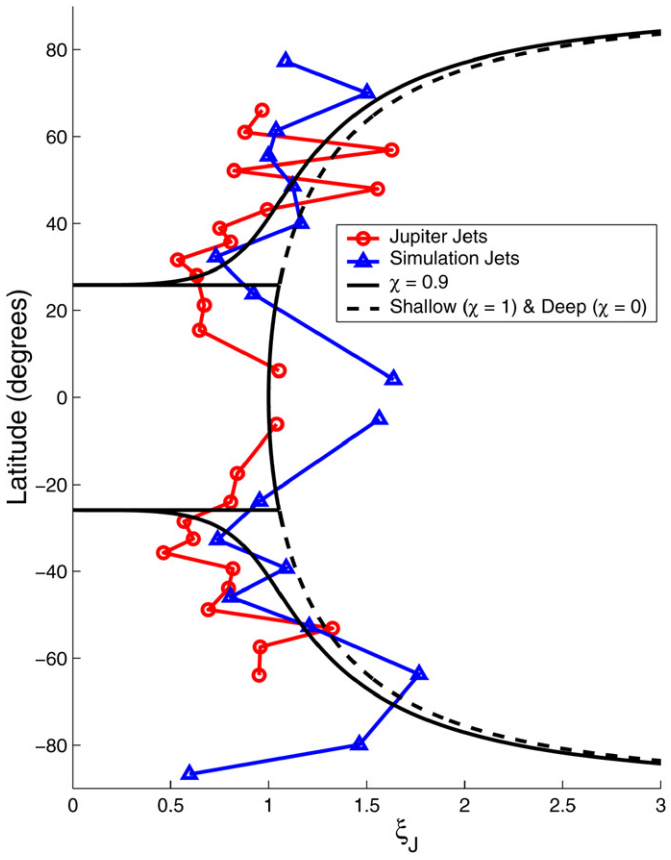

Fig. 12. Measured values of ξ_J, given by (17), for the zonal jets of Jupiter (red) and the numerical model (blue). The values of ξ_J are obtained from the mean azimuthal jet velocities $\langle |u| \rangle$, with the mean taken over all longitudes and the latitude range corresponding to the measured width $\lambda_J/2$ of each jet. See text and Fig. 7 for explanation of jet measurement. The solid black curve is the function $\xi(\theta)$, given by (15) and (16), with $\chi = 0.9$. The tangent cylinder is seen to correspond to a discontinuity in $\xi(\theta)$, and thus to a discontinuity in the jet scaling. The dashed curve shows $\xi(\theta)$, given by (15), for the β-plane approximation, which is equivalent, outside the tangent cylinder, to $\xi(\theta)$ for $\chi = 0.9$, or any value of χ (see also Fig. 6). (For interpretation of the references to color in this figure ledend, the reader is referred to the web version of this article.)

and outside the tangent cylinder:

$$C(\chi) = \frac{1}{\pi/2 - \cos^{-1}\chi} \int_{\cos^{-1}\chi}^{\pi/2} \frac{\sin\theta\cos\theta}{\sqrt{\chi^2 - \cos^2\theta}}\, \mathrm{d}\theta$$
$$= \frac{\chi}{\pi/2 - \cos^{-1}\chi}; \quad |\theta| \geqslant \cos^{-1}\chi, \tag{21}$$

$$C(\chi) = \frac{1}{\cos^{-1}\chi} \int_{0}^{\cos^{-1}\chi} \cos\theta\, \mathrm{d}\theta$$
$$= \frac{\sin(\cos^{-1}\chi)}{\cos^{-1}\chi}; \quad |\theta| \leqslant \cos^{-1}\chi. \tag{22}$$

Here we see that $C(\chi)$ has different values inside and outside the tangent cylinder. Equation (20), with $C(\chi)$ calculated exactly by (21) and (22), gives us a direct mapping from

Table 3
Comparison of regionally averaged values of measured jet widths $\langle \lambda_J/2 \rangle$ (the brackets indicate regional averaging) to the geostrophic Rhines width $\lambda_g/2$ and the β-plane Rhines width $\lambda_\beta/2$

Region	Latitude range	Jupiter				Numerical model ($\chi = 0.9$)			
		$\langle U \rangle$ (m/s)	$\langle \lambda/2 \rangle$	$\lambda_g/2$	$\lambda_\beta/2$	$\langle U \rangle$ (m/s)	$\langle \lambda/2 \rangle$	$\lambda_g/2$	$\lambda_\beta/2$
North	25.8°–90.0°	7.5	4.3°	5.0°	6.3°	20.2	7.6°	8.2°	10.4°
Equatorial	−25.8°–25.8°	57.7	9.3°	12.6°	12.6°	105.3	19.7°	17.0°	17.0°
South	−90°–25.8°	9.7	4.4°	5.7°	7.2°	26.7	8.6°	9.4°	11.9°
Global	−90.0°–90.0°	22.7	5.5°	9.7°	9.7°	46.9	10.7°	14.0°	14.0°

Notes. The North and South regions represent latitudes inside the tangent cylinder, while the Equatorial region lies outside the tangent cylinder. The zonal scaling velocity U for each of three regions is used to obtain the corresponding Rhines widths $\lambda_g/2$ and $\lambda_\beta/2$, which are plotted in Fig. 13. The Rhines width $\lambda_g/2$ for each region is calculated from (20) using the regional scaling velocity U. For $\chi = 0.9$ (the value used in our numerical simulation), (21) and (22) yield $C = 0.804$ inside the tangent cylinder and $C = 0.966$ outside the tangent cylinder. The values of λ_β in the North and South regions correspond to the three limiting cases: (1) β-plane approximation or (2) $\chi = 0$ or (3) $\chi = 1$. The value $C(\theta_\chi) = 0.504$ is derived for these limiting cases using the equivalent spherical shell radius ratio $\chi = 0.9$ [see text and Eq. (22)]. The global Rhines scaling has the single geometric parameter value $C = 2/\pi$.

the regionally averaged scaling velocities to the corresponding regional Rhines wavelengths. Having obtained the regional Rhines wavelengths, they can be substituted back into (18) to obtain $U(\theta)$. Fig. 6 shows, in addition to the raw velocity profile and jet boundaries, the scaling velocity profiles

$$U(\theta) = \frac{\langle U \rangle}{C(\chi)} \frac{1}{\xi^2(\theta)} = \langle U \rangle \frac{1/\xi^2(\theta)}{\langle 1/\xi^2(\theta) \rangle}, \tag{23}$$

that use the mean velocities $\langle U \rangle = \langle |u| \rangle$ of each region (north, equatorial, and south) for the $\chi = 0.9$ numerical model results and for Jupiter.

As discussed above, geostrophic flow in a spherical shell effectively segregates into the three regions (north, south and equatorial) bounded by the tangent cylinder. Because the limiting cases (full sphere and shallow layer) lack a tangent cylinder, there is no physical basis for regionally segregating the flow fields in the β-plane approximation. It follows that the limiting cases are consistent with a single Rhines length, which is obtained using the global scaling velocity and the limiting value $C = 2/\pi$ [obtained either from (21) with $\chi = 1$ or, alternatively, from (22) with $\chi = 0$]. However, models based on these limiting cases (Yano et al., 2003, 2005; Williams, 1978; Cho and Polvani, 1996), obtain relatively fast equatorial flow, compared to that at higher latitudes. Thus, because the Rhines scale depends upon the scaling velocity, it seems appropriate to calculate the Rhines scaling in the β-plane approximation based on regionally (rather than globally) averaged scaling velocities. In this case we separate the full sphere or shallow layer into regions (north, equatoria and south) as for the case of a spherical shell. The latitude $\theta_\chi = \cos^{-1}\chi$ bounds the equatorial region of a full sphere or shallow layer, which corresponds to the intersection of the tangent cylinder with the outer surface for an "equivalent" spherical shell of radius ratio χ. Because β-plane and geostrophic Rhines scaling are equivalent outside the tangent cylinder, the β-plane C-value for latitudes less than θ_χ is the same as that for the equivalent spherical shell. The β-plane value for latitudes greater than θ_χ is denoted $C^*(\theta_\chi)$ and has a possible range $0 < C^*(\theta_\chi) < 2/\pi$. Its value is given by

$$C^*(\theta_\chi) = \frac{1}{\pi/2 - \theta_\chi} \int_{\theta_\chi}^{\pi/2} \cos\theta \, d\theta$$

$$= \frac{1 - \sin(\theta_\chi)}{\pi/2 - \theta_\chi}; \quad |\theta| \geqslant \theta_\chi. \tag{24}$$

Thus, the β-plane approximation, applied to a spherical surface zonal flow at latitudes $\theta_\chi \geqslant 25.8°$, yields the value $C^*(\theta_\chi) = 0.504$, where $\chi = 0.9$ refers to the radius ratio of an "equivalent" spherical shell. Fig. 13 compares the measured jet widths against the theoretical Rhines widths based on regionally and globally averaged zonal velocities for Jupiter and for the $\chi = 0.9$ numerical model. Table 3 also gives the regional and global Rhines widths based on the β-plane approximation.

5. Jet scaling on Saturn

Saturn has a strong prograde (eastward) equatorial jet and features three prograde high latitude jets in each hemisphere. Thus its jet pattern is comparable, but with faster and broader jets, to that of Jupiter. However, contrary to the jovian jets, some of which are strongly retrograde, saturnian jets seem to be almost purely prograde, with a minimum retrograde velocity of −15 m/s compared with the maximum equatorial jet velocity of 470 m/s and the maximum higher latitude jet velocity of 145 m/s (for the jet centered on 42 °N). Furthermore, a decrease in the rotational period the Saturn's kilometric radio (SKR) emissions measured by the Cassini mission relative to that measured by Voyager (Sanchez-Lavega, 2005; Porco et al., 2005), which has been interpreted as a decrease in the planetary rotation rate, shifts the jet velocities even more prograde. The measured increase of 1% in the SKR emissions period implies that Saturn's jets are entirely prograde. This variability throws into question the use of SKR emissions as an estimate of the planetary rotation rate. The uncertainty in the rotation rate also propagates uncertainty into the measurement of jet width (since the jet width is typically estimated in relation to zero relative velocity) and the calculation of saturnian Rhines scaling (since the scaling velocity U depends on the relative velocity and factors into the Rhines scale).

Despite these uncertainties, we can estimate the regional Rhines lengths for Saturn using the latitudinal velocity profiles based on Voyager and Cassini data (Fig. 1) and using the standard planetary rotation rate based on Voyager radio emissions. We assume that the breadth of Saturn's equatorial jet reflects

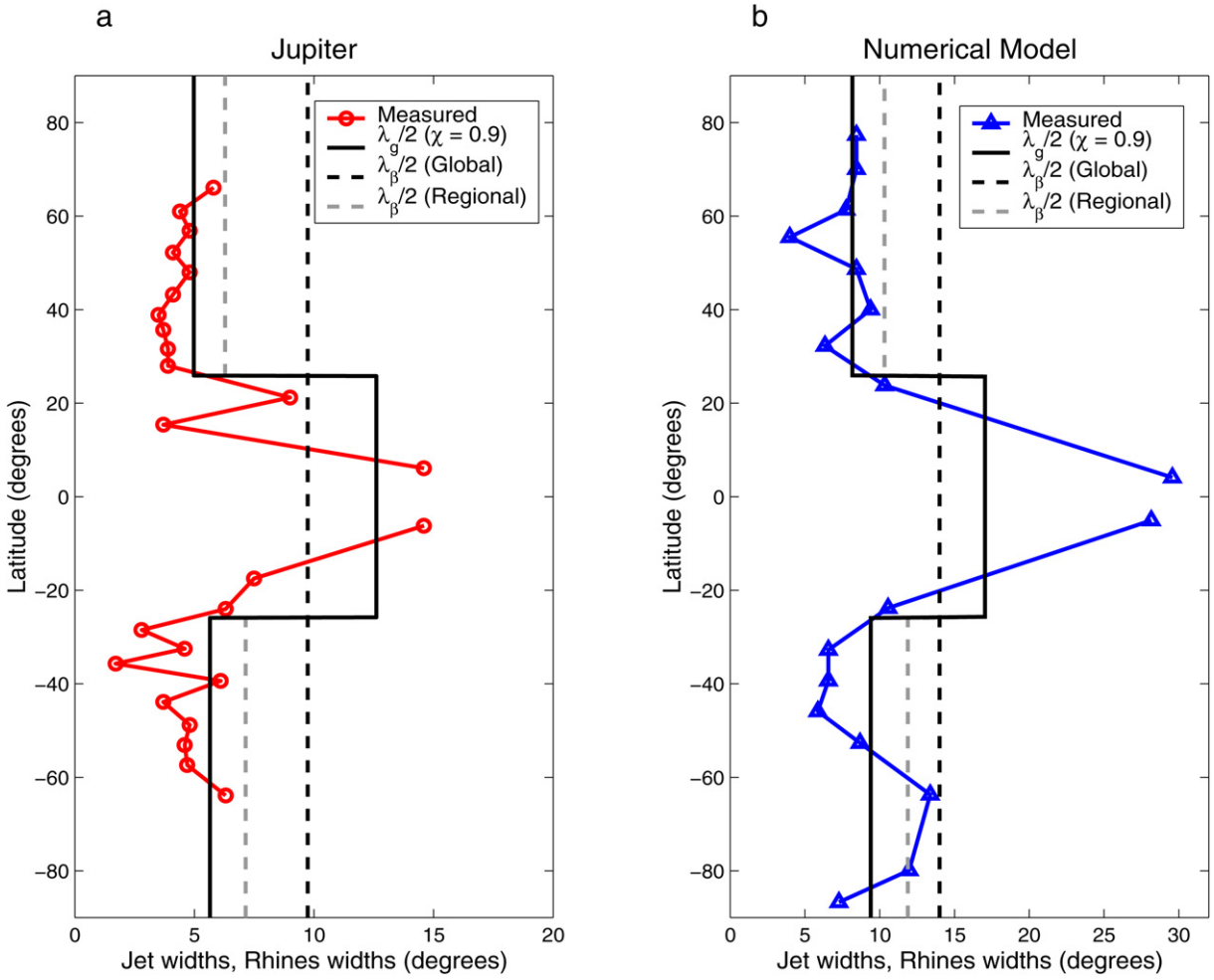

Fig. 13. Measured jet widths compared to Rhines widths for (a) Jupiter and (b) the numerical model. The circle and triangle symbols each represent a jet measurement. The equatorial jet width is estimated on both sides of the equator (see Fig. 7). Geostrophic Rhines widths $\lambda_g/2$ (solid black lines) are obtained from (20), using the observed zonal scaling velocities for each of the three regions bounded by the tangent cylinder (north, equatorial and south). The dashed black (gray) lines represent the β-plane Rhines widths $\lambda_\beta/2$ from the global (regional) mean of the zonal velocity magnitude. Outside the tangent cylinder (i.e., the equatorial region) the geostrophic and β-plane approximations are equivalent such that $\lambda_g = \lambda_\beta$.

Table 4
Estimated jet widths compared to Rhines widths assuming a radius ratio $\chi = 0.8$ for deep saturnian zonal flow

Region on Saturn	Latitude range	$\langle U \rangle$ (m/s)	$\langle \lambda/2 \rangle$	$\lambda_g/2$	$\lambda_\beta/2$
North	37°–90.0°	64.7	8–15°	15.7°	22.3°
Equatorial	−37°–37°	244.7	50–70°	29.5°	29.5°
South	−90°–37°	65.2	8–15°	15.8°	22.4°
Global	−90.0°–90.0°	177.0	–	30.4°	30.4°

Note. Notation is similar to that in Table 3.

the location of the tangent cylinder. Taking this approach, a radius ratio of $\chi = 0.8$ results from placing the boundary between equatorial and high latitude jets at 37° latitude. Table 4 compares estimates of the saturnian jet widths with those predicted by geostrophic and β-plane Rhines scaling. The scaling velocities in the northern and southern hemispheres (above 37° latitude) are 64.7 and 65.2 m/s, respectively—highly symmetrical. Using (20) the resulting Rhines widths are roughly $\lambda_g = 16°$ in each hemisphere (15.7° and 15.8° in the north and south, respectively). The jet width estimate of 16° is consistent the observed three prograde jets between latitudes of roughly 37°–77° in each hemisphere. In the equatorial region the scaling velocity for latitudes less than 37° is 245 m/s. Again using (20), this results in a Rhines width of $\lambda_g = 29.5°$.

6. Discussion

The numerical experiments presented here show that the coexistence of a prograde equatorial jet and multiple higher latitude jets can arise from deep convection in a spherical shell. Furthermore, our scaling analysis predicts that zonal flow in a spherical shell contains a strong increase in the width of zonal jets across a scaling discontinuity that corresponds to the intersection of the tangent cylinder with the outer surface. The fact

that this theoretical scaling discontinuity is reproduced in the numerical models, as well as observed on Jupiter and Saturn, represents strong evidence that the surface zonal flow extends deeply into the molecular envelope (or deep atmosphere) but not throughout the interiors of the gas giants. The termination of deep zonal flow structures likely results from increasing fluid density and electrical conductivity with depth. However, the nature of the layering in the interior of Jupiter and Saturn is far from certain, as is the precise depth of fast zonal flow.

Our results suggest that the depth of fast zonal flow can be estimated by analyzing the latitudinal variation of jet widths. We have shown that for Jupiter, a zonal flow depth of one tenth of Jupiter's radius, which represents a radius ratio $\chi = 0.9$, seems plausible (see Figs. 10, 12, 13). However, the range of plausible radius ratios is perhaps $0.85 < \chi < 0.95$, which corresponds to a range of latitudes $31.8° < \theta_{TC} < 18.2°$, where θ_{TC} represents the position of the tangent cylinder (and the scaling discontinuity) at the planetary surface. Comparing the zonal flow profiles produced by our numerical models with that of Jupiter we see that our models all feature a single strong prograde jet with two flanking retrograde jets in the equatorial region (Fig. 3) while Jupiter's equatorial wind profile is richer in complexity, with a strong dimple at the equator, a higher latitude prograde jet of similar maximum velocity to that of the equatorial jet, and an asymmetric and strong retrograde jet flanking the equatorial jet to the South (Fig. 1a). In addition, recent Cassini fly-by measurements revealed small-scale azimuthal flows above $\pm 70°$ latitude. Similar small-scale flows do not develop in our models.

In our numerical models we do not obtain multiple jets at equatorial latitudes outside the tangent cylinder. For the $\chi = 0.9$ case, the equatorial jet has an estimated latitudinal width of over 30°—roughly twice the predicted Rhines width. Thus, the equatorial region does not seem to follow Rhines scaling theory. Rather, the jet width seems to be controlled by the size of the equatorial region. Multiple jets tend to form inside the tangent cylinder because the lower flow velocity at higher latitudes translates into a smaller Rhines scale there. In addition, larger radius ratios decrease the Rossby number, which is proportional to the zonal flow velocity, thus further decreasing the Rhines scale (Fig. 3). Finally, thinner shells provide a larger latitudinal extent within the tangent cylinder for multiple jets to form.

Based on our theory for Rhines scaling in a spherical fluid shell, equatorial jets are expected to be broader than high latitude jets. However, the tendency for equatorial jets in our simulations (and perhaps on Jupiter and Saturn) to be broader than the predicted equatorial Rhines width may have to do with a fundamental difference between flow dynamics inside and outside the tangent cylinder. Rhines scaling theory relies on an asymptotic expansion of the Navier–Stokes equation under the assumption of geostrophy. However, such an expansion is not strictly justified where the boundary slope becomes large relative to equatorial plane (Busse, 1970; Yano, 1992; Yano et al., 2005). Such is the case near the equator, where the surface boundary is perpendicular to the equatorial plane. Furthermore, Christensen (2002) pointed out that it is not clear how multiple jets can form outside the tangent cylinder, since even multiple turbulent convection cells there produce Reynolds stress in the same prograde direction. The theoretical and numerical difficulties presented by multiple prograde jets outside the tangent cylinder are obviated if the effective radius ratio of Jupiter is 0.95. In that case, only the equatorial jet along with the flanking retrograde jets exist outside the tangent cylinder.

We have chosen to focus mainly on comparing our numerical and theoretical results to the wind profile of Jupiter, rather than that of Saturn. The reason for this is that we chose our input parameters to obtain a Rossby number close to that of the surface winds of Jupiter in the $\chi = 0.9$ case. Also, Jupiter has enough jets to make feasible a detailed analysis of the latitudinal variation of its zonal flow, and its zonal flow pattern is remarkably stable, having varied little between the missions of Voyager and Cassini. Analysis of Saturn's zonal flow pattern is complicated by uncertainty in the planetary rotation rate (see discussion in Section 5). Nevertheless, the saturnian zonal wind profile bears a strong resemblance to the flow patterns resulting from our simulations with $\chi = 0.85$ and $\chi = 0.9$. Saturn's equatorial jet has a relatively simple structure compared to the equatorial region of Jupiter. Disregarding the difficulties presented by the uncertainty in planetary rotation rate, it seems plausible to estimate the effective radius ratio for saturnian zonal flow to be roughly in the range $0.8 \lesssim \chi \lesssim 0.9$, based on the width of the equatorial jet. It is also noted that Rhines scaling, which we have used to explain jet scaling, is in qualitative agreement with the proportional increase in the zonal wind velocity and roughly two-fold broadening of jets between Jupiter and Saturn.

While our models seem to capture the main features of the zonal flow patterns of Jupiter and Saturn, we can only speculate as to what our results can tell us about the significant differences between the two planets. For example, what accounts for the observation that Saturn's zonal flow is more strongly prograde than that of Jupiter? This has been attributed to stronger basal coupling on Saturn (Aurnou and Heimpel, 2004). In that numerical modeling study, cases with a rigid bottom boundary yielded a strong prograde equatorial jet with weak and mainly prograde high latitude jets, such that the mean zonal flow was strongly prograde. However, to produce relatively strong high latitude jets with those boundary conditions will require a lower Ekman number than is implemented here. What is the nature of the coupling between zonal flow in the deep atmosphere and flow in the metallic, dynamo source region? Implicit in our spherical shell model is the assumption that there exists a transition from fast zonal flow to more sluggish flow in the deep interior. It is thought that such a transition is likely to be sharper for Saturn than for Jupiter, for which there is evidence of present-day active differentiation (Hubbard et al., 1999; Guillot et al., 2004). Progress on this question may be critical to explain the differences between the two planets as well as the apparent change in the rotation rate of Saturn.

References

Al-Shamali, F.M., Heimpel, M.H., Aurnou, J.M., 2004. Varying the spherical shell geometry in rotating thermal convection. Geophys. Astrophys. Fluid Dynam. 98, 153–169.

Atkinson, D.H., Pollack, J.B., Seiff, A., 1998. The Galileo Probe Doppler Wind Experiment: Measurement of the deep zonal winds on Jupiter. J. Geophys. Res. 103, 22911–22928.

Aubert, J., Brito, D., Nataf, H.-C., Cardin, P., Masson, J.P., 2001. A systematic experimental study of spherical shell convection in water and liquid gallium. Phys. Earth Planet. Int. 128, 51–74.

Aubert, J., Gillet, N., Cardin, P., 2003. Quasigeostrophic models of convection in rotating spherical shells. Geochem. Geophys. Geosyst. 4, 1052.

Aurnou, J.M., Heimpel, M.H., 2004. Zonal jets in rotating convection with mixed mechanical boundary conditions. Icarus 169, 492–498.

Aurnou, J., Andreadis, S., Zhu, L., Olson, P., 2003. Experiments on convection in Earth's core tangent cylinder. Earth Planet. Sci. Lett. 212, 119–134.

Aurnou, J.M., Olson, P.L., 2001. Strong zonal winds from thermal convection in a rotating spherical shell. Geophys. Res. Lett. 28, 2557–2559.

Brun, A.S., Toomre, J., 2002. Turbulent convection under the influence of rotation: Sustaining a strong differential rotation. Astrophys. J. 570, 865–885.

Busse, F.H., 1970. Thermal instabilities in rapidly rotating systems. J. Fluid Mech. 44, 441–447.

Busse, F.H., 1976. A simple model of convection in the jovian atmosphere. Icarus 20, 255–260.

Busse, F.H., 2002. Convective flows in rapidly rotating spheres and their dynamo action. Phys. Fluids 14, 1301–1314.

Cho, J.Y.-K., Polvani, L.M., 1996. The morphogenesis of bands and zonal winds in the atmospheres on the giant outer planets. Science 273, 335–337.

Christensen, U.R., 2001. Zonal flow driven by deep convection on the major planets. Geophys. Res. Lett. 28, 2553–2556.

Christensen, U.R., 2002. Zonal flow driven by strongly supercritical convection in rotating spherical shells. J. Fluid Mech. 470, 115–133.

Christensen, U., Olson, P., Glatzmaier, G.A., 1999. Numerical modelling of the geodynamo: A systematic parameter study. Geophys. J. Int. 138, 393–409.

Evonuk, M., Glatzmaier, G.A., 2004. 2D studies of various approximations used for modeling convection in the giant planets. Geophys. Astrophys. Fluid Dynam. 98, 241–255.

Giampieri, G., Dougherty, M.K., 2004. Rotation rate of Saturn's interior from magnet field observations. Geophys. Res. Lett. 31, doi:10.1029/2004GL020194.

Gillet, N., Jones, C.A., 2006. The quasi-geostrophic model for rapidly rotating spherical convection outside the tangent cylinder. J. Fluid Mech. 554, 343–369.

Glatzmaier, G.A., 1984. Numerical simulations of stellar convective dynamos. I. The model and the method. J. Comput. Phys. 55, 461–484.

Glatzmaier, G.A., 2005a. Planetary and stellar dynamos: Challenges for next generation models. In: Soward, A.M., Jones, C.A., Hughes, D.W., Wiess, N.O. (Eds.), Fluid Dynamics and Dynamos in Astrophysics and Geophysics. CRC Press, Boca Raton, FL, pp. 331–357.

Glatzmaier, G.A., 2005b. A saturnian dynamo model. In: American Geophysical Union Fall Meeting 2005, San Francisco, CA.

Glatzmaier, G.A., Roberts, P.H., 1995. A three-dimensional convective dynamo solution with rotating and finitely conducting inner core and mantle. Phys. Earth Planet. Int. 91, 63–75.

Guillot, T., Stevenson, D.J., Hubbard, W., Saumon, D., 2004. The interior of Jupiter. In: Bagenal, F., Dowling, T.E., McKinnon, W.B. (Eds.), Jupiter, the Planet, Satellites and Magnetosphere. Cambridge Univ. Press, Cambridge, pp. 35–57.

Hammel, H.B., de Pater, I., Gibbard, S., Lockwood, G.W., Rages, K., 2005. Uranus in 2003: Zonal winds, banded structure, and discrete features. Icarus 175, 534–545.

Heimpel, M., Aurnou, J., Wicht, J., 2005. Simulation of equatorial and high-latitude jets on Jupiter in a deep convection model. Nature 438, 193–196.

Hubbard, W.B., Guillot, T., Marley, M.S., Burrows, A., Lunine, J.I., Saumon, D.S., 1999. Comparative evolution of Jupiter and Saturn, Planet. Space Sci. 47, 1175–1182.

Ingersoll, A.P., 1976. Pioneer 10 and 11 observations and the dynamics of Jupiter's atmosphere. Icarus 29, 245–253.

Ingersoll, A.P., Pollard, D., 1982. Motion in the interiors and atmospheres of Jupiter and Saturn: Scale analysis, anelastic equations, barotropic stability criterion. Icarus 52, 62–80.

Ingersoll, A.P., Dowling, T.E., Gierasch, P.J., Orton, G.S., Read, P.L., Sanchez-Lavega, A., Showman, A.P., Simon-Miller, A.A., Vasavada, A.R., 2004. Dynamics of Jupiter's atmosphere. In: Bagenal, F., Dowling, T.E., McKinnon, W.B. (Eds.), Jupiter, the Planet Satellites and Magnetosphere. Cambridge Univ. Press, Cambridge, pp. 105–128.

Jones, C.A., Rotvig, J., Abdulrahman, A., 2003. Multiple jets and zonal flow on Jupiter. Geophys. Res. Lett. 30, doi:10.1029/2003GL016980.

Kirk, R.L., Stevenson, D.J., 1987. Hydromagnetic constraints on deep zonal flow in the giant planets. Astrophys. J. 316, 836–846.

Kuang, W.-J., Bloxham, J., 1999. Numerical modeling of magnetohydrodynamic convection in a rapidly rotating spherical shell: Weak and strong field dynamo action. J. Comput. Phys. 153, 51–81.

Manneville, J.B., Olson, P., 1996. Banded convection in rotating fluid spheres and the circulation of the jovian atmosphere. Icarus 122, 242–250.

Pedlosky, J., 1979. Geophysical Fluid Dynamics. Springer-Verlag, New York.

Pirraglia, J.A., 1984. Meridional energy balance of Jupiter. Icarus 59, 169–176.

Porco, C.C., and 23 colleagues, 2003. Cassini imaging of Jupiter's atmosphere, satellites and rings. Science 299, 1541–1547.

Porco, C.C., and 34 colleagues, 2005. Cassini imaging science: Initial results on Saturn's atmosphere. Science 307, 1243–1247.

Read, P.L., Yamazaki, Y.H., Lewis, S.R., Williams, P.D., Miki-Yamazaki, K., Sommeria, J., Didelle, H., Fincham, A., 2004. Jupiter's and Saturn's convectively driven banded jets in the laboratory. Geophys. Res. Lett. 31, doi:10.1029/2004GL020106.

Rhines, P.B., 1975. Waves and turbulence on a beta-plane. J. Fluid Mech. 69, 417–443.

Russell, C.T., Yu, Z.J., Kivelson, M.G., 2001. The rotation period of Jupiter. Geophys. Res. Lett. 28, 1911–1912.

Sanchez-Lavega, A., 2005. How long is the day on Saturn? Science 307, 1223–1224.

Sanchez-Lavega, A., Rojas, J.F., Sada, P.V., 2000. Saturn's zonal winds at cloud level. Icarus 147, 405–420.

Sanchez-Lavega, A., Hueso, R., Perez-Hoyos, S., 2004. Observations and models of the general circulation of Jupiter and Saturn. In: Ulla, A., Manteiga, M. (Eds.), Lectures, Notes and Essays in Astrophysics. Universidad de Vigo, Vigo, Spain, pp. 41–63.

Schoff, R., Colin de Verdiere, A., 1997. Taylor columns between concentric spheres. Geophys. Astrophys. Fluid Dynam. 86, 43–73.

Stanley, S., Bloxham, J., 2004. Convective-region geometry as the cause of Uranus' and Neptune's unusual magnetic fields. Nature 428, 151–153.

Sun, Z.-P., Schubert, G., Glatzmaier, G.A., 1993. Banded surface flow maintained by convection in a model of the rapidly rotating giant planets. Science 260, 661–664.

Vasavada, A.R., Showman, A.P., 2005. Jovian atmospheric dynamics: An update after Galileo and Cassini. Rep. Prog. Phys. 68, 1935–1996.

Vorobieff, P., Ecke, R., 2002. Turbulent rotating convection: An experimental study. J. Fluid Mech. 458, 191–218.

Wicht, J., 2002. Inner-core conductivity in numerical dynamo simulations. Phys. Earth Planet. Int. 132, 281–302.

Williams, G.P., 1978. Planetary circulations. 1. Barotropic representation of jovian and terrestrial turbulence. J. Atmos. Sci. 35, 1399–1426.

Williams, G.P., 2003. Jovian dynamics. Part III. Multiple, migrating, and equatorial jets. J. Atmos. Sci. 60, 1270–1296.

Yano, J.-I., 1992. Asymptotic theory of thermal convection in rapidly rotating systems. J. Fluid Mech. 243, 103–131.

Yano, J.I., Talagrand, O., Drossart, P., 2003. Origins of atmospheric zonal winds. Nature 421, 36.

Yano, J.I., Talagrand, O., Drossart, P., 2005. Deep two-dimensional turbulence: An idealized model for atmospheric jets of the giant outer planets. Geophys. Astrophys. Fluid Dynam. 99, 137–150.